Molecular Cell

Article

# The 3D Topography of Mitotic Chromosomes

## Graphical Abstract

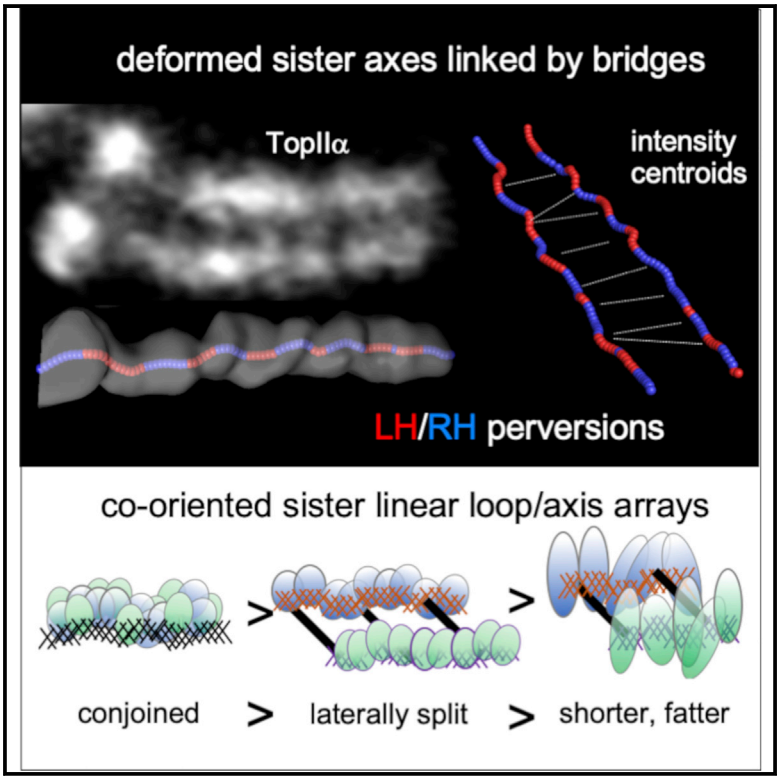


## Highlights

- DNA/structure bridges link sister chromatid axes to stabilize mitotic chromosomes
- Mitotic chromosomes comprise co-oriented linear loop/axis arrays that linearly shorten
- Mitotic chromosomes are not helically coiled
- Chromosome axes are sequential half-helices of alternating handedness (perversions)

## Authors

Lingluo Chu, Zhangyi Liang, Maria Mukhina, ..., John Hutchinson, Denise Zickler, Nancy Kleckner

## Correspondence

kleckner@fas.harvard.edu

## In Brief

Split sister axes of mitotic chromosomes are linked by "mini-axis" bridges that provide mechanical stability. Existence of bridges precludes helical chromosome coiling. Instead, unsplit prophase linear loop/axis arrays, with deformed axes comprising sequential half-helical segments of alternating handedness (perversions), undergo lateral splitting and then compact via simple linear shortening.

Chu et al., 2020, Molecular Cell *79*, 1–15
September 17, 2020 
https://doi.org/10.1016/j.molcel.2020.07.002

CellPress

Please cite this article in press as: Chu et al., The 3D Topography of Mitotic Chromosomes, Molecular Cell (2020), https://doi.org/10.1016/j.molcel.2020.07.002

Molecular Cell

CellPress

Article

# The 3D Topography of Mitotic Chromosomes

Lingluo Chu,[1] Zhangyi Liang,[1] Maria Mukhina,[1] Jay Fisher,[1,2] Nadine Vincenten,[1] Zheng Zhang,[1,3] John Hutchinson,[4] Denise Zickler,[5] and Nancy Kleckner[1,6,*]

[1]Department of Molecular and Cellular Biology, Harvard University, Cambridge, MA, USA
[2]Redbud Labs, Research Triangle, NC 27709, USA
[3]CAS Key Laboratory of Quantitative Engineering Biology, Shenzhen Institute of Synthetic Biology, Shenzhen Institutes of Advanced Technology, Chinese Academy of Sciences, Shenzhen, People's Republic of China
[4]School of Engineering and Applied Sciences, Harvard University, Cambridge, MA, USA
[5]University Paris-Saclay, CEA, CNRS, Institute for Integrative Biology of the Cell (I2BC), Gif sur Yvette, France
[6]Lead Contact
*Correspondence: kleckner@fas.harvard.edu
https://doi.org/10.1016/j.molcel.2020.07.002

## SUMMARY

A long-standing conundrum is how mitotic chromosomes can compact, as required for clean separation to daughter cells, while maintaining close parallel alignment of sister chromatids. Pursuit of this question, by high resolution 3D fluorescence imaging of living and fixed mammalian cells, has led to three discoveries. First, we show that the structural axes of separated sister chromatids are linked by evenly spaced "mini-axis" bridges. Second, when chromosomes first emerge as discrete units, at prophase, they are organized as co-oriented sister linear loop arrays emanating from a conjoined axis. We show that this same basic organization persists throughout mitosis, without helical coiling. Third, from prophase onward, chromosomes are deformed into sequential arrays of half-helical segments of alternating handedness (perversions), accompanied by correlated kinks. These arrays fluctuate dynamically over <15 s timescales. Together these discoveries redefine the foundation for thinking about the evolution of mitotic chromosomes as they prepare for anaphase segregation.

## INTRODUCTION

Mitotic chromosomes prepare themselves for anaphase segregation by undergoing progressive organization and sister chromatid separation, ultimately appearing as short, fat, parallel sister units suitable for clean separation to daughter cells (Figure 1A). This progression begins with the emergence of chromosomes as discrete, cytologically visible objects, at prophase. By mid-prophase, chromosomes are long and thin and are morphologically single, despite the presence of two (closely conjoined) sister chromatids (Liang et al., 2015) (Figure 1B). Sister chromatids then individualize, during a late prophase transition stage (Liang et al., 2015; Nagasaka et al., 2016). Finally, during prometaphase and metaphase, side-by-side sister chromatids become progressively shorter, wider, and denser to give the final compact pre-anaphase configuration. The underlying nature(s) of these events have been of intense interest since chromosomes were first visible by light microscopy.

Sister chromatids are organized as intimately comingled, co-oriented linear arrays of loops that emanate from a single conjoined structural axis meshwork (Figure 1C) (Liang et al., 2015). This organization, recently elucidated for mitotic prophase (Liang et al., 2015), has been known for decades for meiotic prophase chromosomes (Figure 1D) (for review, see Zickler and Kleckner, 1999). The chromatin matrix and the structural axis are both complex DNA/DNA/protein/protein meshworks of connections, along and between sister chromatids (Kleckner, 2006; Marko, 2011; Poirier and Marko, 2002; Sun et al., 2018).

The nature of chromosome morphogenesis after prophase is more mysterious. Ever since mitotic chromosomes were first examined, it has often been assumed that they become shorter and fatter because they undergo helical coiling (for review, see Manton, 1950). This inference emerged largely from images of fixed chromosomes (Manton, 1950; Ohnuki, 1965, 1968) (Figure 1E). It was given detailed support by the seminal work of Laemmli (Marsden and Laemmli, 1979; Maeshima et al., 2005), whose EM images suggested that chromatin loops emanating radially from a helically coiled axis (i.e., by helical coiling of a single linear loop/axis array) (Figure 1F). More recently, molecular chromosome conformation capture (HiC) data revealed that genomically distant sequences were in close physical contact (Gibcus et al., 2018). This effect was modeled to imply that, similar to the model of Laemmli, sequential loops emerge radially from a relatively straight axis, like the steps of a helical staircase emerging from a central strut (Figure 1G). Additional features suggested that loop sizes increase progressively as compaction proceeds, and increased density reflects additional intra-loop folding (Gibcus et al., 2018).

All models that invoke helical coiling of individual chromatids raise a basic conundrum: how does such coiling, along an individual chromatid, accommodate the presence of a closely associated (linked) sister chromatid (Figure 1H)? This issue is not

Please cite this article in press as: Chu et al., The 3D Topography of Mitotic Chromosomes, Molecular Cell (2020), https://doi.org/10.1016/j.molcel.2020.07.002



widely discussed. If individual chromatids do undergo helical coiling, then connections at the sister/sister interface must be dynamically adjustable (Piskadlo et al., 2017). If, instead, sister connections were stable, then helical coiling would cause the two chromatids to "torque" around one another, resulting in plectonemic intertwining. Such intertwining is not observed and would, in any case, be incompatible with simple sister separation at anaphase. This challenge could be solved if sisters somehow "folded" rather than coiling. The possibility of folded (rather than helically coiled) topologies for metaphase chromosomes has been raised by several studies (Giménez-Abián et al., 1995; Kireeva et al., 2004; Marko, 2011).

The present study was initiated to address the above conundrum. The fundamental issues at hand are macroscopic and morphological in nature. We therefore applied high resolution 3D fluorescence imaging of whole chromosomes in living and fixed mammalian cells, along with a novel approach involving analysis of chromatin and axis centroid paths. These investigations have led to three main discoveries that, together, provide a new view of the topology and morphogenesis of mitotic chromosomes.

## RESULTS

### Sister-Chromatid Axes Are Linked by "Mini-Axis" DNA/Structure Bridges

Imaging of the major chromosome axis component topoisomerase IIα (TopIIα) reveals that sister chromatids are linked by inter-axis bridges. These bridges are observed in living pig cells (LLC-Pk EGFP-TopIIα) and by immunofluorescence analysis of fixed cells (e.g., of muntjac [DM87] and human [HeLa]) (Figures 1I–1K and S1A–S1D). Bridges emerge concomitant with sister individualization at late prophase and are present thereafter. They are evenly spaced along the chromosomes, at a distance between adjacent bridges of ~400 nm, and reduce in number as chromosomes shorten, while nonetheless retaining their characteristic even spacing (see below). Bridges disappear during anaphase at "forks" of separation (Figure 1I), raising the possibility that they may be the final target of the anaphase separation process, as addressed in a future report.

Bridges also contain other known post-prophase axis components. Condensin I and condensin II (Skibbens, 2019; Sun et al., 2018) are both present, as seen in both living and fixed cells (Figures 2A–2D and S1E–S1M). Bridges also contain SMC6 (member of the SMC5/6 complex) (Gómez et al., 2013) (Figure 2E) and architectural component HMG1/Y (Saitoh and Laemmli, 1994) (Figure 2F).

In addition, bridges contain Rad21, the kleisin component of the cohesin complex (Figures 2G and 2H). This is especially notable because bulk cohesin is present on prophase axes but is lost from the axes when sisters split at late prophase (Liang et al., 2015; Waizenegger et al., 2000). Moreover, in the presence of non-cleavable cohesin, chromosomes progress through an attempted anaphase, but with bridges remaining present (Figures 2I and S2A). Thus, cleavage during anaphase is required for removal of bridges. These effects underlie previous observations that cohesin is present at the sister/sister interface after prophase, and its cleavage is required for successful anaphase separation (Giménez-Abián et al., 2004; Nakajima et al., 2007).

Bridges also contain chromatin, again as seen in both living and fixed cells (Figures 2J–2M and S2B–S2E). Moreover, when sister chromatid DNAs are differentially labeled with bromodeoxyuridine (BrdU) and 5-ethynyl-2′-deoxyuridine (EdU), bridges are apparent in total staining (Figure 2M, top), and each bridge can be seen to contain DNA from both sisters, with the two DNAs emanating inward across each bridge (Figure 2M, bottom).

Given their composition, these DNA/structure bridges can be considered "miniature axes." We envision that sister chromatid loops are catenated (Figure 2N) and bound by structural components (Figure 2O), ultimately appearing along continuous, parallel bridge-linked sister axes (Figure 2P). The presence of cohesin, a prophase axis component, plus TopIIα and condensin II, which are also present at that time, suggest that bridges may evolve directly from prophase axes. This inference is directly validated by further studies presented below.

Literature-searching identified several images of inter-sister bridges (Giménez-Abián et al., 1995; Jane, 1934; Ohnuki, 1968; Sumner, 1998a, 1998b). However, the existence of these bridges was commented upon by the author(s) in only one of these studies, some 80 years ago (Jane, 1934), before any possible discussion of molecular components.

### Mitotic Chromosomes Comprise Parallel Co-oriented Linear Loop/Axis Arrays Whose Axes Are Regularly Deformed by Half-Helical Segments of Alternating Handedness and Partially Correlated Kinks

Bridges are stable inter-sister linkages, as documented directly below. The existence of such bridges thus challenges the notion that mitotic chromosomes are helically coiled (Introduction). We therefore re-investigated the organization of compacting prometaphase/metaphase chromosomes by visualizing their chromatin and TopIIα axis shapes and defining their centroid paths (Figures 3A and 3B). Each such shape was sliced along its length; the intensity-weighted centroid was determined for each slice; and path of these centroids along the length of the shape was defined. Each path was then analyzed to determine whether, at each position along its length, there is any tendency for helicity and, if so, whether that helicity is left-handed or right-handed.

#### *Chromatid Axes Exhibit Regular Half-Helical Perversions with Net Zero Handedness Accompanied by Kinks*

Centroid analysis of TopIIα paths reveals that the axes of prometaphase/metaphase chromosomes are not helically coiled, contrary to some previous proposals (Figures 1F–1H). Instead, axis paths are substantially planar and comprise a sequential array of approximately half-helical segments of alternating handedness (red/blue). This pattern also includes periodic "kinks," i.e., positions at which there is an abrupt change in the slope of the path (white dots). These kinks tend to be regularly spaced and often, but not always, occur at the positions of handedness changes. There is also a tendency for adjacent segments to be slightly rotated relative to one another (Figures 3C, 3E, and 3G, right). Half-helical segments are ~200 nm in length, with a subset of longer length segments, and with left- and right-handedness occurring at equal frequency (Figures 3D, S3A, S3B, and S3G). Strikingly, the path defined by centroid analysis can also be

Please cite this article in press as: Chu et al., The 3D Topography of Mitotic Chromosomes, Molecular Cell (2020), https://doi.org/10.1016/j.molcel.2020.07.002



CellPress

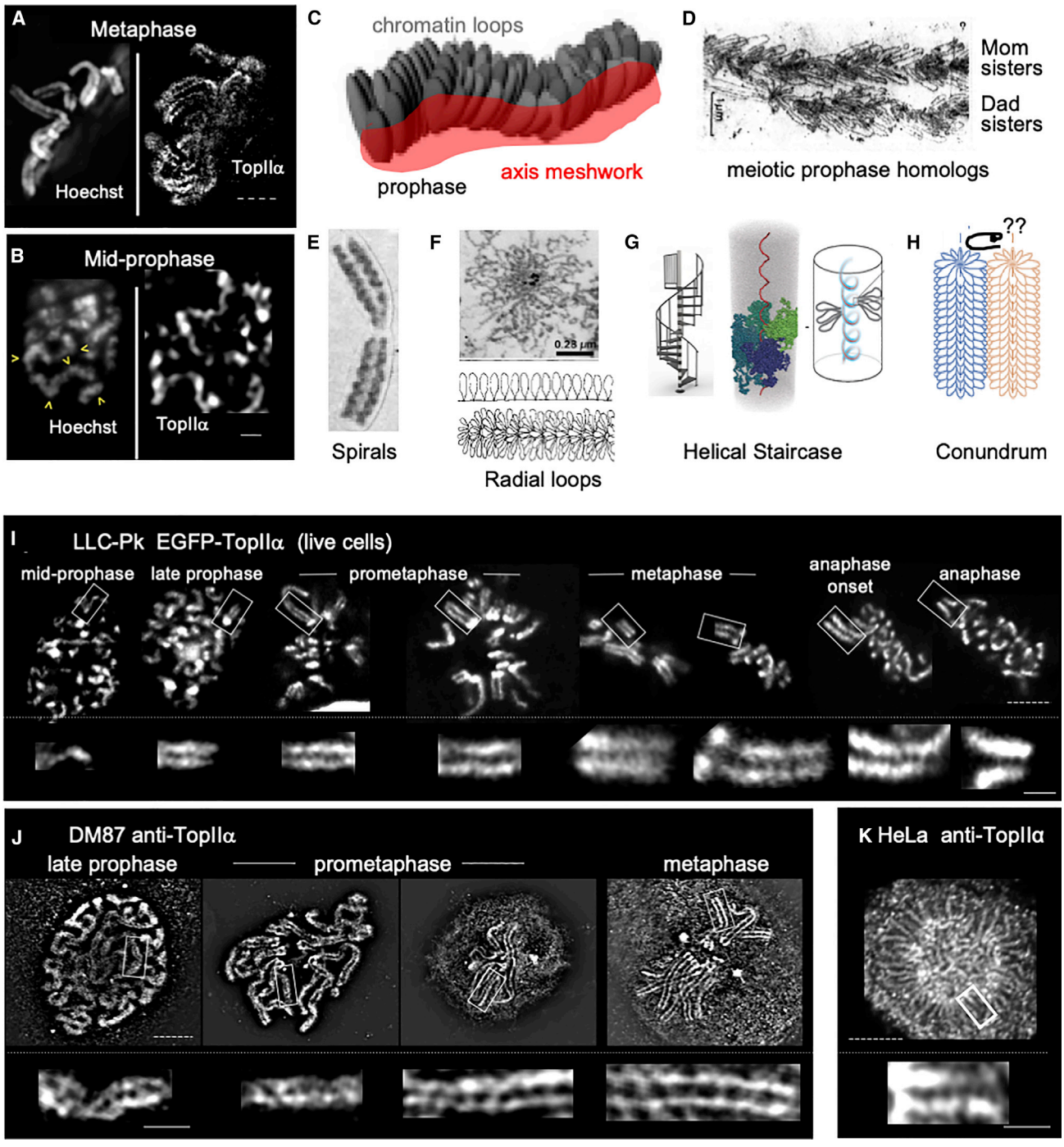


**Figure 1. Mitotic Chromosomes and Bridges**

(A and B) DM87 prophase chromosomes fluorescently stained for DNA (Hoechst) and axes (TopIIα). Yellow arrows in (A) denote major kinks (from Liang et al., 2015). Dense TopIIα staining regions are centromeres.

(C) Mitotic prophase chromosomes are organized as co-oriented, closely conjoined sister linear loop/axis arrays.

(D) Meiotic prophase chromosomes exhibit closely conjoined co-oriented sister linear loop/axis arrays along each homolog (from Keyl, 1975).

(E–G) Previous findings interpreted as evidence for helical coiling along metaphase chromosomes: apparent "spirals" along colchicine-treated human chromosomes (E) (Ohnuki, 1965); radial loops emanating from a helically-coiled linear loop axis array (F) (bottom: Marsden and Laemmli [1979]; top: Maeshima et al. [2005]); and helical staircase coiling model derived by polymer simulations of HiC data (G) (Gibcus et al., 2018).

(H) Conundrum: how does helical coiling accommodate the presence of parallel linked sister chromatids?

(I–K) Sister chromatid axes are linked by evenly spaced bridges from late prophase through anaphase as revealed by localization of TopIIα in living cells (I) and fixed cells (J and K) of different indicated mammalian cell lines. Additional examples in Figures S1A–S1D. Scale bars, 1 μm, solid lines; 5 μm, dashed lines.

Please cite this article in press as: Chu et al., The 3D Topography of Mitotic Chromosomes, Molecular Cell (2020), https://doi.org/10.1016/j.molcel.2020.07.002



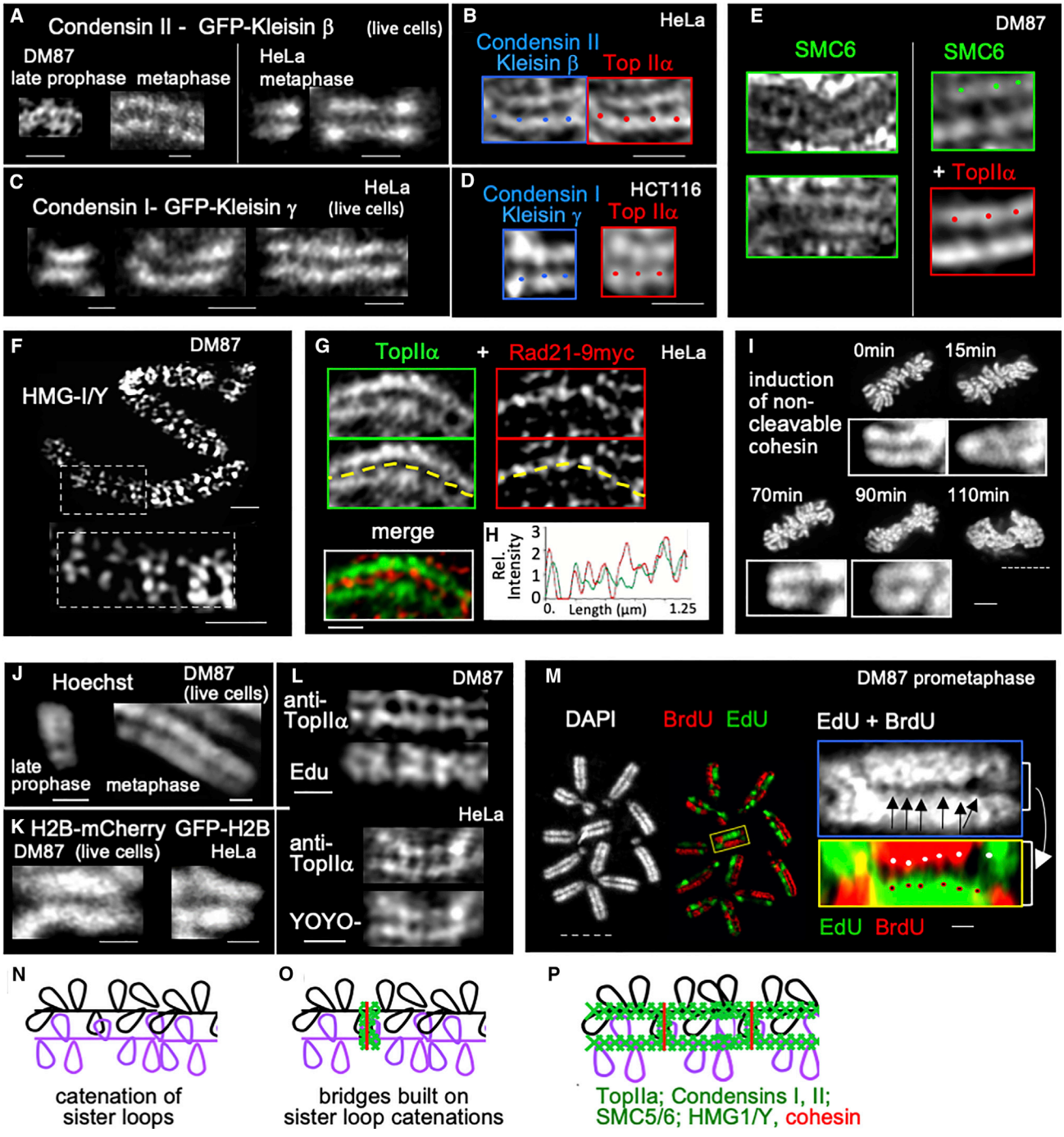


**Figure 2. Bridges between Sister Chromatids Are Miniature Axes**

(A–F) Post-prophase bridges contain the multiple indicated known chromosome axis components as defined in living and fixed cells of several types, in co-localization with TopIIα bridges (additional examples in Figures S1E–S1M).

(G and H) Bridges also contain residual Rad21, which is no longer present along the main axes.

(I) Cleavage of this residual cohesin is required for loss of bridges at anaphase (details in Figure S2A).

(J–L) Bridges also contain chromatin as seen by DNA stains or fluorescently tagged histone H2B (living and/or fixed cells).

(M) Sister chromatids were differentially labeled by sequential exposure to BrdU and EdU (details in STAR Methods). Color switches along main axes are attributable to BrdU-induced sister chromatid exchange. Right: bridges (arrows and circles) are each seen to comprise DNA emanating from both sisters. Weaker signals likely represent nonspecific catenation of sister loops that will inevitably be present due to nonspecific action of TopIIα.

*(legend continued on next page)*

Please cite this article in press as: Chu et al., The 3D Topography of Mitotic Chromosomes, Molecular Cell (2020), https://doi.org/10.1016/j.molcel.2020.07.002



seen directly in overall axis shape (Figure 3E). These findings imply that chromatid axes are deformed with a tendency for local helicity. However, that helicity is manifested segmentally in only (approximately) half of a helical turn and alternates in handedness along the length of the chromosome. As a result, axis paths overall are-topologically "neutral," with net zero twist and lack any global helical coiling. An approximate rendering of such a path is shown in Figure 3G.

The nature of the TopIIα axis path described above is further validated by two further observations.

First, the observed path can be distinguished experimentally from that for a simple helix by analysis of 3D "z stacks" through the shape (Figures 3H and 3I). For a simple helix, the segments in different planes change orientation from top to bottom within the stack (Figure 3H). From some perspectives, the axis shapes observed in this study exhibit regular series of bulges that might be taken to indicate a helical path. In fact, these bulges generally correspond to the positions of handedness changes (Figure 3I). Moreover, Z section analysis shows that axis segments exhibit the same orientation in all planes, as expected from our identified path (Figures 3I and S2F).

Second, the axis path has the unique feature that it exhibits duality of intensity because the positions of handedness change move from side to side along the shape (Figure 3G, left). In fact, exactly such intensity duality is directly visible in the chromatin shape of living chromosomes, as a manifestation of the underlying axis path (Figure 3J; below) and, similarly, in the chromatin morphologies of spread fixed chromosome preparations (Figures 3K and S2G). Interestingly, anaphase chromosomes in living Haemanthus cells also exhibit sub-chromatid duality (Bajer, 1965), which observation occasioned extensive discussion as to whether a chromatid comprises one DNA molecule or two. The current findings resolve this decades-old controversy.

A switch in helical handedness is an interesting geometric feature termed a "perversion." Discovery of perversions along mitotic chromatid axes provides unique elucidation of this geometry in a eukaryotic biological system at the subcellular level (Discussion).

We further find that there is a direct relationship between the pattern of deformations along chromosome axes and the positions of bridges. First, bridges tend to emerge from the positions of inward-facing bulges (turquoise dots, Figure 3E, top images), which usually correspond positions of handedness changes (compare with corresponding below images; quantification in Figures S3C and S3D). Second, bridges are quite uniformly spaced along the axes, with a distance between adjacent bridges of ~400 nm and a shape parameter for the best-fit Gaussian distribution of $\nu = 6$ (Figures 3F and S4; below). Because half-helical axis segments are ~200 nm in length (above and Figure 3D), adjacent bridges should, on average, be separated, along each axis, by two half-helical segments. These relationships point to a cause-and-effect relationship between deformations and bridges. Analyses to be presented elsewhere suggest that this correspondence reflects direct mechanical linkage between axis deformations and events of the bridge emergence process (L.C., Z.L., M.M., J.H., and N.K., unpublished data).

### *Chromatin and Axis Paths Lie in a Parallel, Paranemic Relationship*

Chromatin and TopIIα axis centroid paths lie in a parallel and paranemic relationship along the entire lengths of individual chromatids (Figures 3L, 3N–3Q, S5A, and S5B). Such a relationship is exactly that expected for a linear loop/axis array where the chromatin emerges from the axis, as at prophase (Figures 3L, right, and 3O, right). Interestingly, the path of the chromatin centroid is related to, but substantially smoother than, that of the axis centroid. A pronounced tendency for back-and-forth twisting of the array over longer length scales is also apparent.

### *Sister Linear Loop/Axis Arrays Are Parallel and Co-oriented*

Centroid analysis also reveals the relationship between the linear loop/axis arrays of sister chromatids. Sister arrays are separated side-by-side, in parallel, and are co-oriented (Figures 3N, 3P, 3Q, S5A, and S5B). This configuration has three important implications. First, bridges can occur along the shared axis surface. Exactly this arrangement is observed (Figures 3N, bottom, 3P, 3Q, S5A, and S5B). Second, from this configuration, chromosomes can shorten by a simple linear process, without helical coiling or any other change in conformation. This is also observed, as further discussed below. Third, this configuration could arise by simple lateral splitting of the tightly conjoined co-oriented linear loop arrays seen along unsplit prophase chromosomes. This pathway is also confirmed below.

Another notable feature of these prometaphase/metaphase chromosomes is that the handednesses at corresponding positions along sister chromatid axes exhibit little or no correlation. This feature is apparent by visual inspection (Figures 3C, 3N, 3P, 3Q, and 6J) and documented quantitatively in Figures S3E–S3H.

All of the above findings apply to chromosomes at all post-prophase stages, from early prometaphase to late metaphase, as well as to chromosomes visualized in both living cells and fixed whole cells (Figures 3N, 3P, 3Q, 6E, below, S3A, S3B, S4, S5A, and S5B).

## Mitotic Chromosome Axis Conformation Is Established during Prophase, Prior to Sister Splitting

The findings presented above pertain to chromosomes in which sister chromatids have separated into individualized units (metaphase/anaphase). This split configuration emerges from the earlier mid-prophase configuration in which sisters are conjoined into a single morphological unit (Introduction). The two configurations are linked by an important transition stage (late prophase) that also includes the concomitant emergence of inter-axis bridges. To investigate the possibility (above) that post-prophase chromosomes arise by lateral splitting of mid-prophase chromosomes, and to understand how bridges emerge as part of this process, we investigated the nature and events of this transition stage.

(N–P) Interpretative models showing topological catenation of sister loops along bridges (N) plus associated axis components (O) and, finally, fully developed late prophase axes linked by mini-axis bridges that contain both prophase and post-prophase axis components (P) and likely have emerged from unsplit prophase axis segments (text). Scale bars, 1 μm, solid lines; 5 μm, dashed lines.

Please cite this article in press as: Chu et al., The 3D Topography of Mitotic Chromosomes, Molecular Cell (2020), https://doi.org/10.1016/j.molcel.2020.07.002



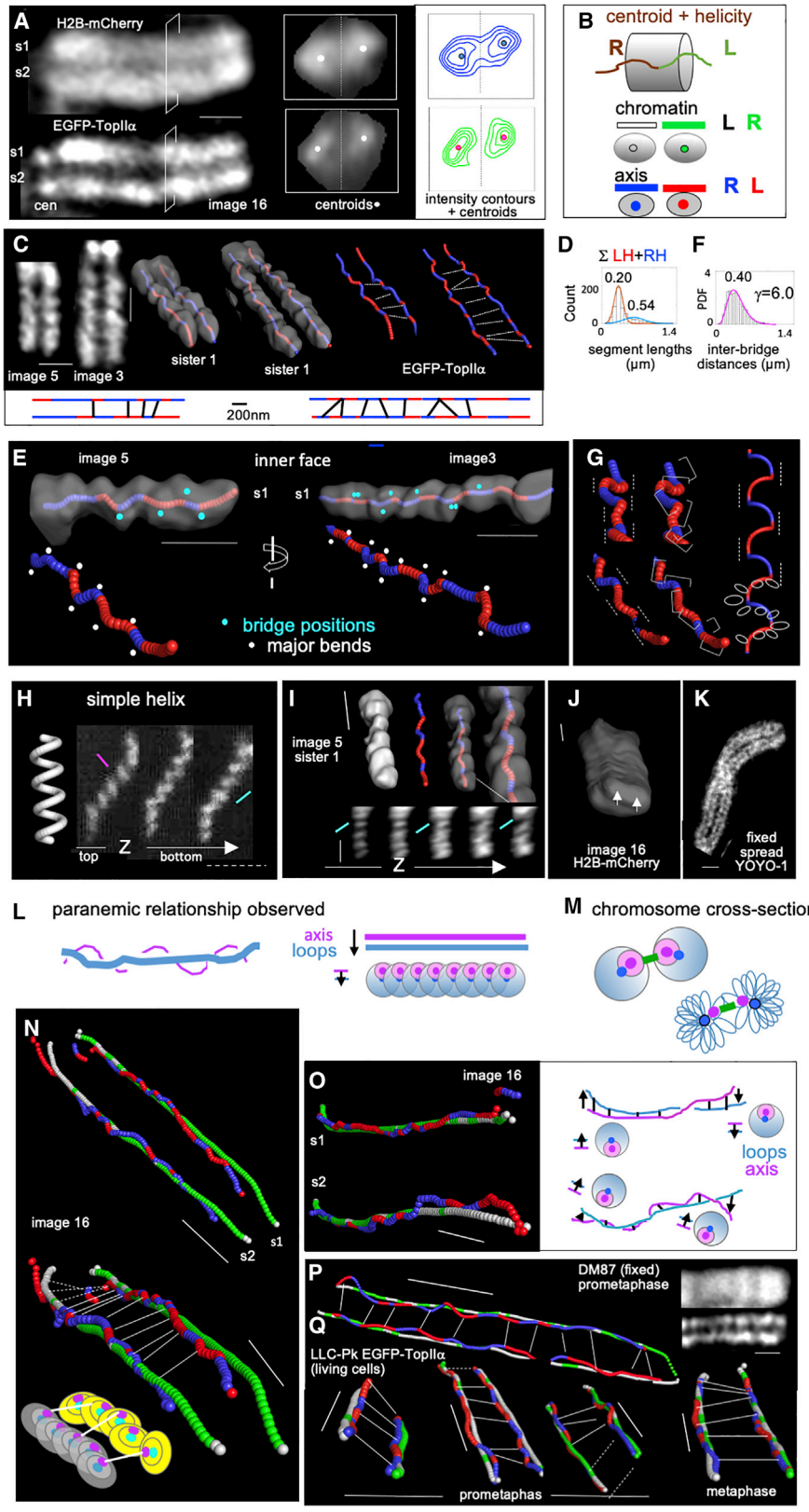


*(legend on next page)*

Please cite this article in press as: Chu et al., The 3D Topography of Mitotic Chromosomes, Molecular Cell (2020), https://doi.org/10.1016/j.molcel.2020.07.002





### Axis Deformations Give Rise to Evenly Spaced Bubbles and Bridges

Images of TopIIα chromosome axes in progressing prophase nuclei (Figures 1C and 4A) allow us to define a morphological pathway for sister splitting and bridge emergence (Figures 4B and 4F). Unsplit prophase axes exhibit occasional very dramatic kinks (yellow arrows in Figures 1C, 4A–4C, and S5D) with intervening regions that may be either more or less deformed. The proportion of more deformed regions is higher at late prophase than at mid-prophase (Figure 4D), implying that deformation accumulates progressively over time.

At the onset of the late prophase transition, axis splitting is triggered by loss of inter-sister (cohesin/catenation) linkages (Giménez-Abián et al., 1995; Liang et al., 2015). Splitting first involves appearance of short "bubbles," after which fully split sister axes linked by bridges emerge (above and Figures 4A and 4B) (Liang et al., 2015). Bubbles tend to be regular in size (~370 nm) (Figures 4E, middle, S4, and S5E) and to occur in close-packed, evenly spaced arrays along the chromosomes (Figures 4D, arrows, S4, and S5E). Correspondingly, the average center-to-center distance between adjacent closely spaced bubbles is ~400 nm, with a gamma distribution shape parameter of $\nu \sim 20$ indicative of even spacing (Figure 4E, left). Newly emerged bridges are also separated along the axes by ~400 nm, again with the same even spacing (gamma distribution shape parameter $\nu \sim 6$–12) (Figures 4E, right, and S4) seen at later stages (above). Together, these findings imply that deformations give rise to closely adjacent, evenly spaced bubbles, with bridges then emerging at the short unsplit positions between adjacent bubbles (Figure 4F). These findings match the evidence described above that bridges evolve from unsplit axis segments at the molecular level.

### Lateral Splitting of Co-oriented Sister Loop/Axis Arrays at Late Prophase

Unsplit prophase chromosomes comprise closely conjoined sister linear loop/axis arrays (Figure 1C; Introduction) (Liang et al., 2015). Correspondingly, along prophase chromosomes, the chromatin

**Figure 3. Organizational Structure of Post-prophase Chromosomes**

(A) Left: representative 3D images of a prometaphase chromosome in a living LLC-Pk cell expressing H2B-mCherry (top) and EGFP-TopIIα (bottom). Middle and right: cross-sectional slices (from position indicated at left) presented as primary images (middle) and intensity contours at 0.6, 0.7, 0.8, and 0.9× maximum image intensity (right). Dots indicate centroids of the respective shapes.

(B) Definition of centroids and centroid paths, and helical handednesses of those paths, for chromatin and axis shapes.

(C) Two LLC-Pk EGFP-TopIIα shapes obtained as snapshots in living cells. Left-to-right: primary images; thresholded PyMOL renderings with corresponding axis centroid paths; axis centroid paths with bridges indicated. Bridge positions were defined as described in STAR Methods (see also Figure 6D).

(D) Distribution of left- and right-handed segment lengths (total) for prometaphase and metaphase chromosome axes in LLC-Pk EGFP-TopIIα live cell snapshots plus two-Gaussian best fit (means = 0.20; 0.54; N = 574 segments). The same distributions are seen for prometaphase and metaphase chromosomes individually and in DM87 (Figure S3B).

(E) Axes of indicated individual chromatids from chromosomes in (C). Top: views of the indicated inner axis faces provided by PyMOL renderings of the thresholded axis shape, plus corresponding centroid paths. Note the close correlation of shape and centroid path and the fact that bridges emerge from curved regions of the shape that emanate toward the other sister (turquoise-filled circles). Bottom: rotated views of axis centroid paths alone showing regularly spaced half-helical segments with handedness changes (red and blue; "perversions") and accompanying regularly spaced kinks (white-filled circles) that occur on alternating sides of the path.

(F) Distribution of inter-bridge distances for prometaphase and metaphase chromosomes in LLC-Pk EGFP-TopIIα live cell snapshots with best fit to gamma distribution (N = 159 segments). The same distribution is seen for prometaphase and metaphase chromosomes individually and in DM87 and HeLa cells (Figure S4).

(G) Perversions along mitotic chromosome axes. Left and middle: enlargements of portions of paths in (E). Note the intrinsic tendency for intensity duality (white dotted lines, left) and for adjacent half-helical segments to be rotated (twisted) relative to one another (brackets, right). Right: cartoon representation of observed path: sequential half-helices of alternating handedness. Right top: duality indicated by white dotted lines. Right bottom: loops disposition.

(H and I) Comparison of paths observed in sequential sections from a 3D z stack for a simple helix (H) and a typical prometaphase axis (I). (H) Ideal simple helix (left) and images of hypercompacted mitotic chromosomes showing changes in segment orientation from top to bottom of the stack (Boy de la Tour and Laemmli, 1988). (I) Prometaphase axis from a chromosome in a living cell (as in C and E). Top, left-to-right: PyMOL renderings of the thresholded axis shape alone, the corresponding axis centroid path, and the path embedded in the thresholded shape with an enlargement. Sequential bulges in the axis shape (left) reflect positions of regular bends with handedness changes (enlargement at right). Bottom: segment orientations do not change from top to bottom of the z stack, contrary to a simple helix. Additional example in Figure S2F.

(J and K) Duality predicted for chromatin according to the consensus path in (G) is manifested in (J) the chromatin shape of one chromatid from the chromosome in (A), shown in a thresholded PyMOL image, and (K) a fixed, spread DM87 chromosome stained with YOYO-1 (entire chromosome complement in Figure S2G).

(L) Paranemic relationship of axis and chromatin centroid paths as predicted for a linear loop/axis array (bottom) and as observed (below).

(M) High resolution imaging shows that chromatin is not smoothly radially dispersed around a central axis as previously envisioned. Intensity contours (A top, middle, and right) show that chromatin density is asymmetrically disposed so as to emanate away from the inter-sister interface. This disposition is illustrated here in cartoons of cross-section of chromosome comprising parallel co-oriented sister linear loop/axis arrays, with axes linked by bridges, and chromatin emanating away from the inter-sister interface. Dark blue and dark purple circles denote centroids of chromatin and axis shapes, respectively, emphasizing appropriate offset as seen by imaging.

(N) Axis and chromatin centroid paths of the chromosome in (A). Top view emphasizes paranemic axis/chromatin relationship (see also O). Bottom view shows positions of bridges, revealing that they link the axes of parallel co-oriented sister linear loop/axis arrays (corresponding cartoon at bottom). Dotted lines are bridges that have trapped a twist along one chromatid.

(O) Alternative views of axis and centroid paths of chromatids in (N), further documenting organization as linear loop/axis arrays with back-and-forth twisting (right).

(P and Q). Additional examples of axis and chromatin centroid paths for segments from prometaphase and metaphase chromosomes from fixed cells (P) and living cells (Q) as indicated. Details of image acquisition and processing are presented in STAR Methods. In brief, chromosomes or chromosome segments that lie in the XY imaging plane were selected and were not subjected to straightening or any other manipulation other than a small amount of in-plane rotation as required for centroid analysis. (C, N, P, and Q) See additional examples and discussion in Figures S5A–S5Z. Scale bars, 1 μm, solid lines.

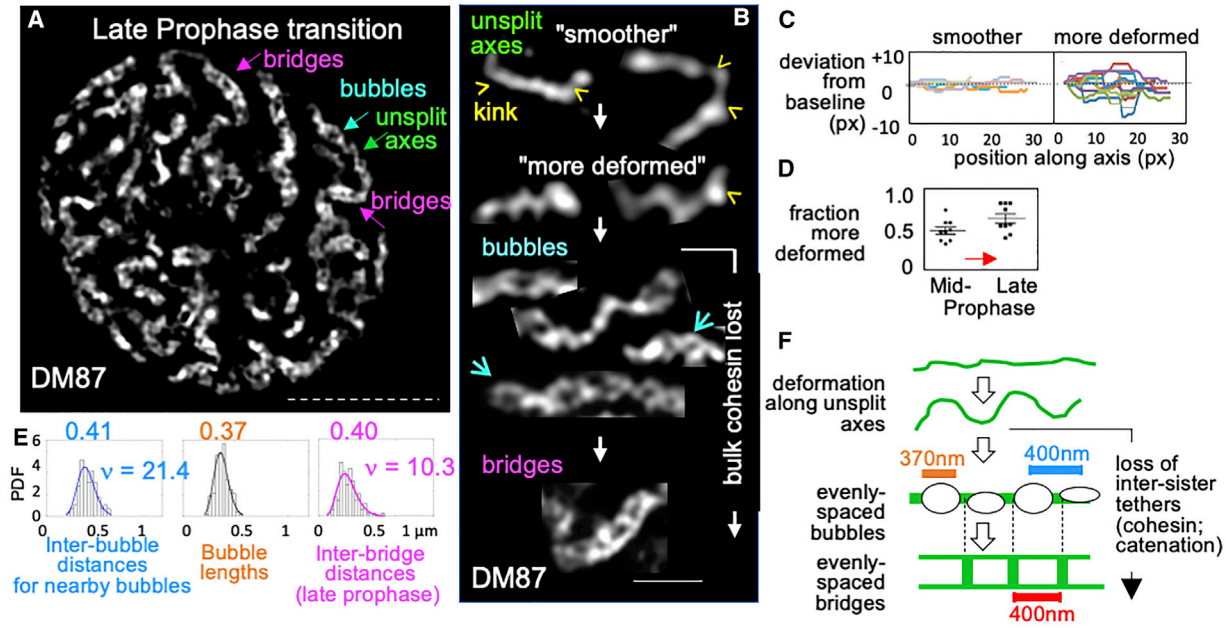


**Figure 4. Morphological Pathway of Progression from Mid- to Late Prophase**

(A) Chromosome axes in a late prophase transition nucleus (DM87 stained with anti-TopIIα).

(B–F) Analysis of DM87 chromosomes stained with anti-TopIIα. The same morphological progression is seen in living LLC-Pk EGFP-opIIα and fixed HeLa cells stained with anti-TopIIα.

(B) Yellow arrows show positions of strong kinks (see also Figure 1A); turquoise arrows indicate examples of closely spaced adjacent bubbles that are rotated relative to one another. Additional examples in Figures S5D and S5E.

(C) Axis shapes can be separated into "smoother" and "more deformed" shapes according to whether the maximum deviation of the center line of the shape from a linear baseline is less or more than ± 3 pixels (left and right, respectively; examples in B).

(D) More deformed segments are more frequent in late prophase nuclei than in mid-prophase nuclei (defined by presence or absence of split axes, n = 7 and 9 nuclei, respectively), implying progressive accumulation of deformation. Note: progression to more deformed shapes is likely greater than it appears because axes with increased deformation are constantly being converted to split axis forms.

(E) Distributions of inter-bridge and inter-bubble distances with best-fit gamma distributions showing even spacing (pink and blue; n = 151 and n = 85). Distribution of bubble lengths showing strong uniformity and size only slightly less than inter-bubble distance, in accord with close juxtaposition of adjacent bubbles (gold; n = 149; Gaussian fit). Data from DM87 fixed whole cells. See also Figure S4.

(F) Pathway of prophase axis morphogenesis (text). Scale bars, 1 μm, solid lines; 5 μm, dashed lines.

centroid path is located peripheral and paranemic to the (deformed) axis path (Figures 5A and S5F). Moreover, just as at post-prophase stages, these axes comprise nearly planar, sequential ~200 nm half-helical segments of alternating handedness and chromatin paths are smoother than axis paths (Figures 5B–5D, 5F, top, S3E–S3H, and S5F). Thus, the conformation of unsplit prophase chromosomes is closely analogous to that seen after sister splitting along individual chromatids at prometaphase/metaphase (Figure 3). Axes of earlier less deformed shapes exhibit fewer, less frequent changes in helical handedness and fewer, less dramatic regions of pronounced curvature than axes of more deformed shapes (Figure 5E), in accord with progressive development of deformations during prophase as seen in whole axis shapes (above, Figure 4D).

Centroid analysis also allows us to further define the splitting process. Bubbles, nascent split regions, and just-emerged bridge-linked sister chromatids exhibit the same diagnostic features of prometaphase/metaphase linear loop/axis arrays: parallel paranemic chromatin/axis paths; axes that comprise sequential ~200 nm half-helical segments of alternating handedness; and evenly spaced inter-axis bridges separated by ~400 nm (Figures 4E, 5G–5J, 5F, bottom, S3E–S3H, and S4).

These findings demonstrate that (1) a fundamental mitotic chromosome conformation, of co-oriented sister linear loop/axis arrays, with axes deformed into sequential half-helices of alternating handedness, is established progressively along unsplit prophase chromosomes (Figure 5A); (2) sister individualization involves lateral splitting of these axes into two parallel linear loop/axis arrays (Figure 5J), as envisioned above; and (3) the basic axis conformation established prior to splitting is maintained during the splitting process and thereafter, throughout prometaphase and metaphase (Figure 3).

We note, however, the paths of unsplit axes appear to have more extreme shape deformations than split axis paths: they appear to be more planar and to exhibit more pronounced kinks. This impression is confirmed by quantitative analysis of axis curvature. The magnitude of curvature is greatest for unsplit axes, decreases somewhat upon splitting to the late prophase state, and then further decreases at prometaphase/metaphase, which are indistinguishable (Figures 5K and 5L).

## Chromosomes Compact by Linear Axis Shortening

Beginning with nuclear envelope breakdown, chromosomes decrease progressively in length (Figures 6A and S6A). They

Please cite this article in press as: Chu et al., The 3D Topography of Mitotic Chromosomes, Molecular Cell (2020), https://doi.org/10.1016/j.molcel.2020.07.002



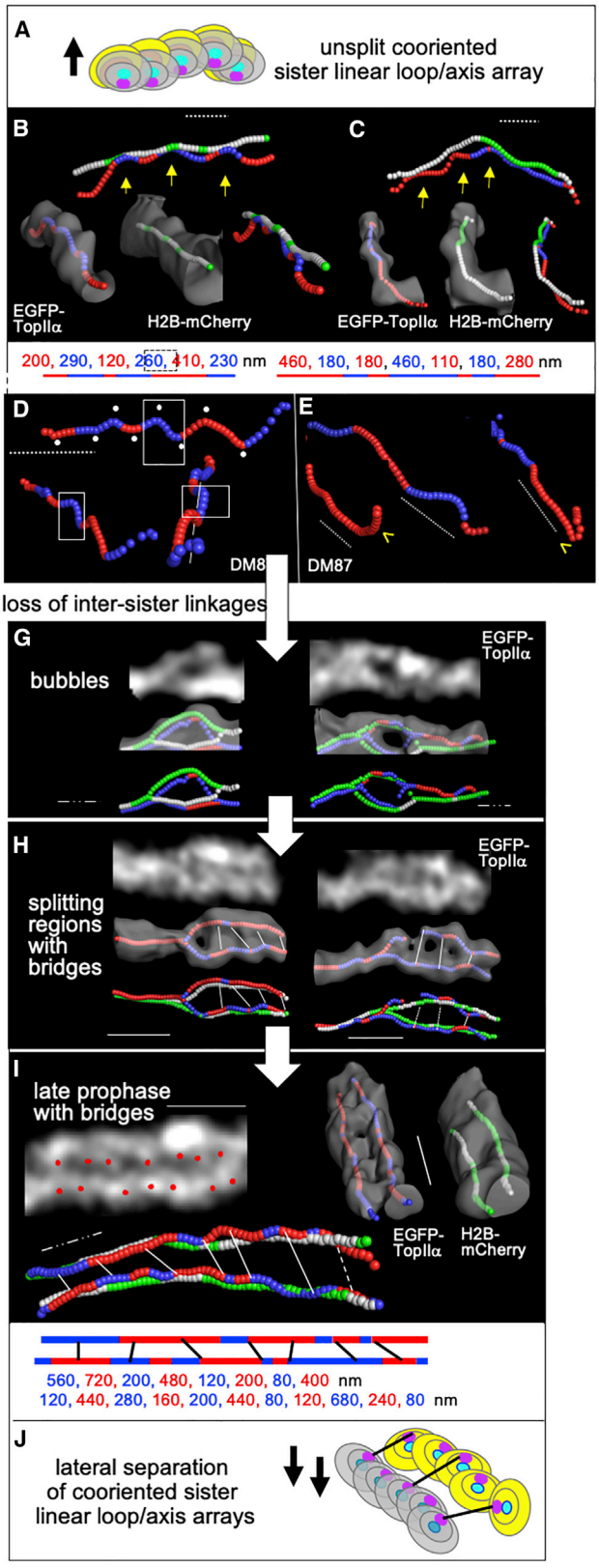


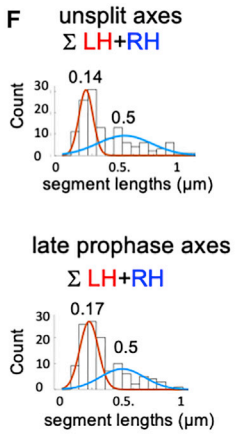


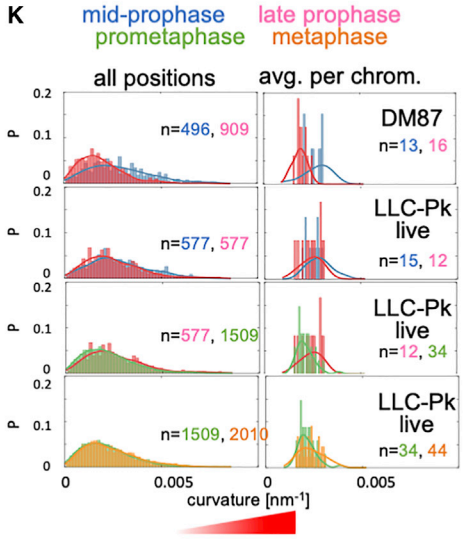


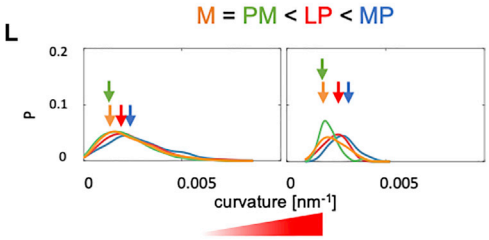


(legend on next page)

Please cite this article in press as: Chu et al., The 3D Topography of Mitotic Chromosomes, Molecular Cell (2020), https://doi.org/10.1016/j.molcel.2020.07.002



concomitantly also become both wider (“fatter”) and denser (Liang et al., 2015).

### *Chromosomes Compact without Any Change in Basic Axis Conformation*

Previous considerations have mostly assumed that these events involve a change in basic chromosome conformation, most notably helical coiling (Introduction). Current observations show that this assumption is not correct. Basic chromosome conformation does not change during the compaction process, as described above (Figures 3 and 5; see also below). Specifically, global helical coiling is not involved. Moreover, because alternating half-helices are present at all times (above) (Figures 6F, 6I, and 6J), their occurrence does not account for chromosome shortening (as could have been the case for helical coiling).

Maintenance of basic conformation is also indicated by the fact that bridges are also always present, with the same ~400 nm spacing of adjacent bridges along the axes, before and during the compaction period, i.e., from late prophase through metaphase, and into anaphase (Figures 3F, 4E, 6B, and S4). Correspondingly, the number of bridges decreases in direct proportion to decreasing end-to-end chromosome length during prometaphase/metaphase (Figure 6C). Time-lapse imaging at 15-s intervals further demonstrates, directly, that bridges are stable during the shortening process (over the timescales available for imaging) except that, sporadically, individual bridges are lost (Figures 6D–6F).

Taken together, these findings lead to the simple conclusion that mitotic chromosomes shorten because their axes shorten, but without any change in basic axis conformation.

Most simply, chromosomes would shorten by a decrease in the number of basic chromatin loops, without any change in loop spacing/density (Kleckner, 2006), and with a concomitant increase in chromatin loop length (Figure 6G). Chromosomes would thereby simultaneously become both shorter and fatter, as observed (Liang et al., 2015; Gibcus et al., 2018). Bridges disappear in correlation with axis shortening, suggesting that they are destabilized by this axis restructuring process.

## Bridges, in Linkage with Sister Chromatid Axes, Provide an Integrated Structure that Stabilizes Mitotic Chromosomes against Disruptive Internal and External Forces

What is (are) the role(s) of bridges? Two potential roles can be excluded. First, bridges are not responsible for creating or maintaining basic axis/chromosome conformation, including features that dictate alternating left- and right-handedness. This basic conformation arises at mid-prophase before bridges are present (above) and thus reflects internal effects that are independent of bridges. Second, bridges do not confer any significant tendency for coordination of handedness along sister chromatids: corresponding pixel positions along sister chromatids exhibit same- and opposite handedness at equivalent frequencies, possibly with a slight preference for opposite handedness (above; Figures 3H and 6G).

In contrast, 3D time-lapse imaging reveals dynamic behaviors that strongly suggest that bridges, in linkage to the two chromatid axes, create an integrated structure that mechanically stabilizes mitotic chromosomes against disruption from internal and external forces.

- Images of TopIIα axes taken every 15 s reveal that both axis shapes and helicity paths are conformationally dynamic on this timescale (or less) (above; Figures 6D–6F) even in the absence of ongoing shortening (Figures 6I and 6J). Changes in handedness over time on sister chromatids are not correlated in any obvious way, in accord with snapshot data (above). Interestingly, chromosomes sometimes fluctuate around a basic consensus conformation: a conformation observed at one moment can disappear 15 s later and then reappear ~100 s later, as seen in both overall shape and axis centroid path (Figure 6K). The basis for these fluctuations remains to be elucidated. They could be thermally driven, as alternate conformations of a mechanically stressed state, and/or actively promoted (ATP-driven). Importantly, sisters remain closely coaligned throughout these dynamic changes (Figure 6I), presumptively due to the presence of bridges (Figure 6E). Accordingly, occasional regions where bridges are absent also show unusual axis separations (Figure 6L).
- In chromosomes that are actively shortening (Figure 6E), sister chromatids decrease in length approximately, but not perfectly, coordinately (Figure 6F). Bridges will tend to keep sister chromatids coaligned throughout the shortening process. In addition, bridges may ensure that sister chromatids shorten to similar extents, as observed. Specifically, an excess of shortening on one of the two chromatids will tend to “pull” on nearby bridges. That effect might, in turn, feed back on axis events to impede further shortening on the more advanced chromatid until the sister could catch up. Consistent with such a scenario, bridges often occur at angles to the two chromatid axes, rather

**Figure 5. Sister Individualization by Lateral Separation of Conjoined Co-oriented Sister Linear Loop/Axis Arrays**

(A and J) Cartoons of unsplit (A) and split (J) co-oriented sister linear loop arrays at mid/late prophase. Arrows indicate the direction of the shared chromatid loop/axis plane (pointing from axis to chromatin).

(B–E and G–I) Bubble/bridge formation. Prophase chromosome progression, as defined by chromatin and/or axis centroid paths, obtained from images of H2B-mCherry and/or TopIIα in living LLC-Pk EGFP-TopIIα cells (B, C, H, and I) or TopIIα defined by immunostaining in fixed DM87 cells (D, E, and G) at the indicated stages. (B–E) Examples of unsplit prophase axes with “more deformed” (B–D) and “smoother” axis paths (E). (G–I) Examples of prophase axes with partial or full splitting. Additional examples in Figure S5F. Yellow arrows in (B) and (C) highlight that axis deformations lie in the loop/axis plane (see also Figure S5F).

(F) Distributions of left- and right-handed axis segment lengths (total) along unsplit and split prophase axes (N = 132 and 118 segments, respectively). Individual handedness distributions in Figures S3D–S3F. Distributions are the same as those observed at prometaphase/metaphase (Figures 3D, S3A, and S3B).

(K and L) The extent of deformation along axes, as defined by curvature magnitude (STAR Methods), is maximal along unsplit axes and then decreases progressively from mid-prophase to late prophase and from late prophase to prometaphase and metaphase, which are not distinguishable. (K) Pairwise comparisons of curvature magnitude distributions at successive stages for all positions (left) and on a per-chromosome basis (right). (L) Comparisons of kernel density estimates for corresponding distributions. Scale bars, 1 μm, solid lines; 0.5 μm, dotted lines.

Please cite this article in press as: Chu et al., The 3D Topography of Mitotic Chromosomes, Molecular Cell (2020), https://doi.org/10.1016/j.molcel.2020.07.002



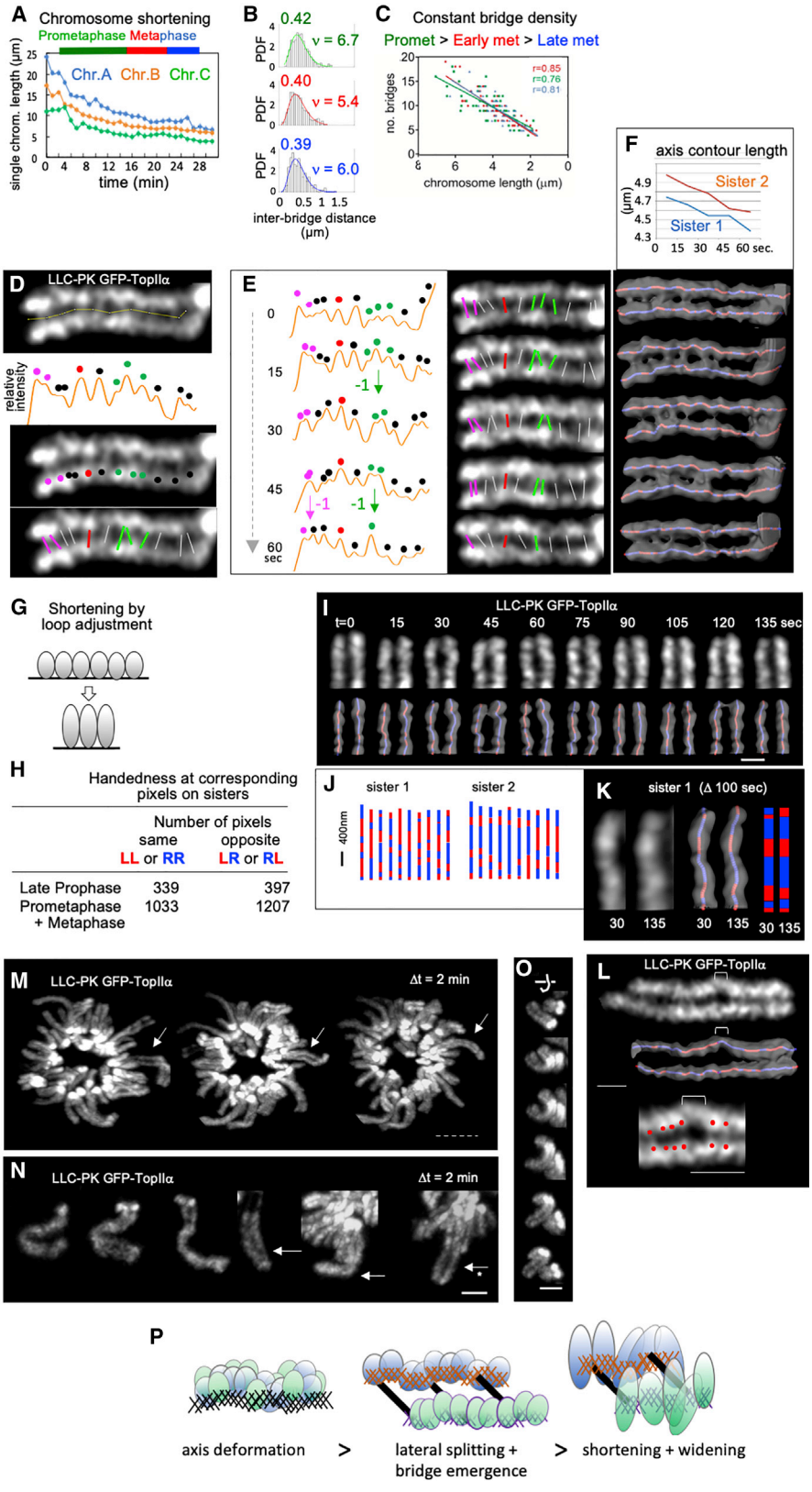


*(legend on next page)*

Please cite this article in press as: Chu et al., The 3D Topography of Mitotic Chromosomes, Molecular Cell (2020), https://doi.org/10.1016/j.molcel.2020.07.002



than being perfectly perpendicular, pointing to differential shortening on the two sisters (examples in Figures 4E and 6E). More generally, from the presented data it seems that shortening may occur in only a few positions at any given time, drawing bridges together in the affected positions until one disappears, without altering spacing of adjacent bridges and without affecting other regions. These effects suggest that bridge disappearance is integrally linked to, and probably driven by, the loop/axis restructuring that underlies chromosome shortening (above).

- Most dramatically, imaging of axes in whole chromosome complements during prometaphase/metaphase reveals that the chromosomes are constantly changing their global shapes, with dramatic curving and twisting, due at least in large part to effects of spindle forces. Nonetheless, at all positions, sister axes remain very closely parallel (Figures 6M–6O, S6C, and S6D). Bridges must be responsible for maintenance of this close alignment.
- Finally, bridges likely play an important role in keeping sisters not only coaligned but with their loop/axis arrays co-oriented. The presence of bridges will prevent the two chromatid shapes from rotating relative to one another along their respective longitudinal axes. This constraint will further contribute to the retention of coherent chromatid structure.

A role of bridges in endowing mitotic chromosomes with mechanical stability is attractive from another perspective. For such an effect, bridges should be evenly spaced at an appropriate distance to minimize the occurrence of large gaps in connectedness. Accordingly, chromosome deformations from both internal and external sources occur over the length scales similar to inter-bridge distances. Thus, satisfyingly, a mechanical role for bridges in maintaining coherence of sister chromatids is precisely the appropriate biological raison d'être for their even spacing and for their specific spacing at ~400 nm.

## DISCUSSION

We began by investigating how sister chromatids compact while remaining closely parallel side-by-side. This investigation has led to several discoveries which, together, provide a new foundation for further investigation of how chromosomes prepare themselves for anaphase segregation.

### Split Sister Chromatid Axes Are Linked by Mini-axis Bridges

Individualized sister chromatids are linked by inter-axis bridges. These bridges are "miniature axes": they contain diverse axis components, as well as chromatin (likely catenated sister loops). Sisters are thus connected robustly, not by flexible chromatin-level catenation/cohesin linkages at their interface. These bridges, in linkage to chromatid axes, provide an integrated structure that stabilizes the sister couple against turbulence from internal forces of compaction and external forces from spindle congression. Bridges are also the ultimate target of anaphase separation (to be described elsewhere).

### A New Organization for Mitotic Chromosomes

We show that (1) each chromatid of a post-prophase mitotic chromosome is organized as a linear array of chromatin loops

**Figure 6. Chromosome Shortening and the Role(s) of Inter-axis Bridges as Defined in Living LLC-Pk EGFP-TopIIα Cells**

(A) Chromosome axes of three individual LLC-Pk EGFP-TopIIα chromosomes, monitored continuously over time from early prometaphase onward, exhibit dramatic shortening during prometaphase and slower shortening once the spindle is established at early (red) and late (blue) metaphase (imaging details in Figure S6A).

(B and C) Bridge spacing remains constant during chromosome shortening.

(B) The distribution of inter-bridge distances is same at all stages (see also Figure 3F) as at late prophase (above; Figure 4E), with even spacing at ~400 nm. Data are from living prometaphase, early metaphase, and late metaphase cells of LLC-Pk EGFP-TopIIα (N = 385, 361, and 369, respectively; see also Figure S4.

(C) The number of bridges per chromosome decreases in proportion to decreasing chromosome length throughout all stages (Pearson's coefficients for linear regression curves shown). Data from LLC-Pk EGFP-TopIIα chromosomes in living cells.

(D–F) Bridge status during 3D time-lapse imaging of single LLC-Pk EGFP-TopIIα axes at 15-s intervals for 60 s.

(D) Bridge positions were defined by intensity profiles along the mid-line between sister chromatids (top two images) and correspond directly to bridge positions discernible by eye (bottom two images).

(E) Bridges are stable over the imaging period except for three instances in which a bridge disappears.

(F) Top: sister chromatid axes shorten significantly during this period, with general but not perfect coordination, as defined by chromatid centroid axis lengths. Bottom: axes fluctuate among various versions of the basic deformed conformation as seen in overall shape and axis handedness patterns (see also I–K).

(G) Loop modulation model for linear chromatid shortening. Loops retain constant density along the axes but become fewer and longer.

(H) Corresponding pixel positions along sister chromatid axis paths exhibit same- and opposite helical handedness with nearly equal frequency. Data from LLC-Pk EGFP-TopIIα chromosomes in living cells. The same results are seen in DM87 fixed whole cells (Figure S3H).

(I–K) 3D time lapse imaging of single LLC-Pk EGFP-TopIIα axes at 15-s intervals for 135 s reveals fluctuations among different versions of the deformed conformation as seen in overall shape (I) and axis handedness patterns (I and J), where (J) is linear representation of segment contour lengths in (I). Notably, in this example, axis contour length does not change during this period. (K) Sister 1 exhibits the same conformation at t = 30 s as at t = 135 s, despite obvious changes in overall shape and axis handedness path during the intervening period.

(L) LLC-Pk EGFP-TopIIα axes of prometaphase chromosome in living cells showing region of axis deformation (white bracket) in which bridges are absent (top; bottom, red dots).

(M–O) Chromosome axes of whole chromosome complements in living LLC-Pk EGFP-TopIIα cells during prometaphase/metaphase. Axes retain close parallel alignment despite dramatic twisting and bending over time (M and N) as seen also by 3D perspectives of a single curved chromosome (O). Asterisk in (N) denotes global sister arm separation characteristic of pre-anaphase (L.C., unpublished data). Full nucleus images for (M) and additional examples in Figures S6C and S6D.

(P) Topological progression of chromosome morphogenesis from prophase to late prophase to metaphase: prophase co-oriented sister linear loop arrays undergo lateral separation that is followed by shortening via reduction in loop number and concomitant increase in loop size. Scale bars, 1 μm, solid lines; 5 μm, dashed lines.

along a robust structural axis meshwork, and (2) sister linear loop arrays are parallel and co-oriented. Thus, contrary to many suggestions over the past century, there is no helical coiling of individual chromatids at any stage. Nonetheless, the presented findings readily accommodate all earlier observations underlying helical coiling models (Boy de la Tour and Laemmli, 1988; Gibcus et al., 2018; Manton, 1950; Marsden and Laemmli, 1979; Ohnuki, 1965, 1968).

- Lower-resolution fluorescence images show chromosome cross-sections with a dense central axis embedded in a cylindrical chromatin shape (Maeshima and Laemmli, 2003), contributing strongly to the notion that chromatin occurs in loops that emanate radially around a central axis (Gibcus et al., 2018; Marsden and Laemmli, 1979). Here, higher resolution images reveal a different picture. Chromatin intensity in cross-sections is neither uniform nor radially symmetric. It has a well-defined border that is not symmetrically circular (Figure 3A). Moreover, for a pair of sisters, chromatin intensity is dramatically reduced in the region between the two chromatid axes. This is expected for co-oriented sister linear loop/axis arrays linked by bridges because chromatin loops will tend to redistribute away from the inter-sister region where there is less room for expansion (Figures 3A, right, and 3N).
- The identified axis, with half-helical segments of alternating handedness, can sometimes give the strong visual impression of regular helical coiling, even in unfixed chromosomes (Figure 3I), as well as after strong classical fixations, which tend to compact the chromatin onto the axes. High-resolution 3D (z stack) analysis, required to distinguish the two cases (above; Figures 3H and 3I), was not available in early studies (Manton, 1950) or was not employed at all (Figure 1E) (Ohnuki, 1965, 1968).
- The presence of alternating helical handedness implies the presence of internal conformational constraints on development of helicity (L.C., Z.L., M.M., J.H., and N.K., unpublished data). Many reports of helical coiling involved chromosome preparations that eliminate such constraints, thus allowing chromosomes to reconfiguration into an unconstrained simple helix in whole chromosome (Boy de la Tour and Laemmli, 1988) and EM "radial loop" images (Figures 1F and 1G).
- Recent HiC data show that sequences separated by large genomic distances are, nonetheless, closely juxtaposed in 3D space, regularly along the chromosomes (Gibcus et al., 2018). Based on polymer modeling, this pattern was interpreted to result from helical "staircase coiling" (Introduction; Figure 1G). However, the motivating experimental feature is equivalently explained by the conformation revealed above: given sequential half-helices of alternating handedness, genomic regions separated by two such segments will come into spatial proximity.

Several previous considerations do not invoke helical coiling. None envisioned the actual chromosome path revealed here. However, a folded path with chromatin peripheral to axes was suggested in a study of chromosome axes in spread preparations (Giménez-Abián et al., 1995). A "hierarchical folding" model was motivated by identification of an ~250 nm diameter folding unit (Strukov et al., 2003), which could correspond to the ~200 nm half helical segments defined directly here. A related study detected no correlation or symmetry between the positions of corresponding spots on sister chromatids (Strukov and Belmont, 2009), in accord with absence of correlations between sister axis path handednesses seen in the current study.

## Progression of Mitotic Chromosomes by Lateral Splitting of Prophase Linear Loop/Axis Arrays to Allow Simple Linear Shortening

We show that, from prophase onward, chromosome status evolves in a very simple way (Figure 6P). The closely conjoined co-oriented sister linear loop/axis arrays present at prophase (Liang et al., 2015) split laterally to give separated, parallel, co-oriented sister arrays with bridges along the shared axis surface. Chromosome compaction then occurs by simple linear shortening of the chromatid axes without any change in basic axis conformation.

Compaction could be economically explained by restructuring of the loop/axis array, to give longer loops and shorter axes without a change in loop spacing along the axes, and with concomitant destabilization of bridges. Mitotic chromosome compaction also involves increased DNA/chromatin density (Liang et al., 2015). Formation of smaller nested loops within the main loops of the loop/axis array (Gibcus et al., 2018; Walther et al., 2018) would explain this effect, as well as explaining repositioning of tagged sequences from the periphery of prophase chromosomes to the interior (axis) of metaphase chromosomes (Dietzel and Belmont, 2001).

## Helical Perversions, Bridges, One-Dimensional Spatial Patterning, and Mechanical Stress

We show that chromosome axes exhibit an unusual and unexpected path: sequential half-helices of alternating handedness (with associated kinks). A switch in helical handedness is an interesting geometric feature termed a "perversion." Mitotic chromosomes provide a unique example of perversions at the subcellular level

Axis perversions are regularly spaced at ~200 nm. Evenly spaced bubbles of axis splitting yield evenly spaced bridges separated by ~400 nm. Both features represent unique examples of one-dimensional spatial patterning and their dimensions point to a direct relationship. Spatial patterning along a physically robust macroscopic object is strongly suggestive of mechanically promoted process(es) (Kleckner et al., 2004) (L.C., Z.L., M.M., J.H., and N.K., unpublished data).

A remaining question raised by the above observations is: why does the deformed axis path, with its perversions and kinks, exist at all? Because the shape and dimensions of the path do not change as chromosomes compact, axis deformations do not constitute a progressive change in geometry that gives rise to shortening (as would be the case for helical coiling). We will propose elsewhere that mechanical stress within chromosome axes creates perversions, targets and promotes formation of bubbles and bridges, and then promotes axis destabilization

as required for chromosome shortening and bridge removal (L.C., Z.L., M.M., J.H., and N.K., unpublished data).

## STAR★METHODS

Detailed methods are provided in the online version of this paper and include the following:

- KEY RESOURCES TABLE
- RESOURCE AVAILABILITY
  - Lead Contact
  - Materials Availability
  - Data and Code Availability
- EXPERIMENTAL MODEL AND SUBJECT DETAILS
  - Cell Lines
  - Standard Growth Conditions
- METHOD DETAILS
  - Synchronization and Inhibitor Treatments
  - Sample Preparation
  - Spread Chromosome Preparations
  - Immuno- and/or DNA staining
  - Imaging and Data Collection
  - Live-cell Imaging
  - Measurement of Distances
  - Image Analysis and Presentation
  - Z direction correction
  - Determination of centroid paths
  - Centroid analysis for different sub-stages
  - Centroid analyses of split shapes
  - Analysis of axis centroid paths
  - Comparison of handednesses between split sister axes (Figures 6H and S3H)
  - Curvature magnitudes of centroid paths (Figures 5K and 5L)
  - PyMOL renderings and PyMOL-centroids superimposition
  - Intensity contour analysis and contour-centroid superimposition
  - Axis, shape and bridge dynamics analysis (Figures 6D–6F and 6I–6K)
  - Volocity and Imaris 3D renderings
  - Statistical Analysis
  - Two-Gaussian analysis of left and right handedness segments (Figures 3D, 5F, S3A, S3B, S3E, and S3F)

## SUPPLEMENTAL INFORMATION

Supplemental Information can be found online at https://doi.org/10.1016/j.molcel.2020.07.002.

## ACKNOWLEDGMENTS

The authors thank T. Hirano, K. Maeshima, J. Ellenberg, G. Gorbsky, M. Kanemaki, Peter Cook, David Lleres, J.V. Shah, and J.-M. Peters for reagents and M. Stouf for MATLAB scripts. We also thank all Kleckner laboratory members and Guido Guidotti for helpful discussions, and J. Henle and B. Weiner for ideas and help with manuscript preparation. This research was supported entirely by grants to N.K. from the NIH (RO1-GM-025326, R01-GM-044794, and R35-GM-136322).

## AUTHOR CONTRIBUTIONS

L.C. and Z.L. collected data. L.C., Z.L., N.K., N.V., M.M, D.Z., Z.Z., and J.H. analyzed data. J.F. created the algorithm for centroid path analysis. All authors participated in preparation and/or editing of the manuscript.

## DECLARATION OF INTERESTS

The authors declare no competing interests.

Received: May 18, 2020
Revised: June 16, 2020
Accepted: July 6, 2020
Published: August 7, 2020

## REFERENCES

Bajer, A. (1965). Subchromatid structure of chromosomes in the living state. Chromosoma *17*, 291–302.

Boy de la Tour, E., and Laemmli, U.K. (1988). The metaphase scaffold is helically folded: sister chromatids have predominantly opposite helical handedness. Cell *55*, 937–944.

Dietzel, S., and Belmont, A.S. (2001). Reproducible but dynamic positioning of DNA in chromosomes during mitosis. Nat. Cell Biol. *3*, 767–770.

Gibcus, J.H., Samejima, K., Goloborodko, A., Samejima, I., Naumova, N., Nuebler, J., Kanemaki, M.T., Xie, L., Paulson, J.R., Earnshaw, W.C., et al. (2018). A pathway for mitotic chromosome formation. Science *35*, eaao6135.

Giménez-Abián, J.F., Clarke, D.J., Mullinger, A.M., Downes, C.S., and Johnson, R.T. (1995). A postprophase topoisomerase II-dependent chromatid core separation step in the formation of metaphase chromosomes. J. Cell Biol. *131*, 7–17.

Giménez-Abián, J.F., Sumara, I., Hirota, T., Hauf, S., Gerlich, D., de la Torre, C., Ellenberg, J., and Peters, J.M. (2004). Regulation of sister chromatid cohesion between chromosome arms. Curr. Biol. *14*, 1187–1193.

Gómez, R., Jordan, P.W., Viera, A., Alsheimer, M., Fukuda, T., Jessberger, R., Llano, E., Pendás, A.M., Handel, M.A., and Suja, J.A. (2013). Dynamic localization of SMC5/6 complex proteins during mammalian meiosis and mitosis suggests functions in distinct chromosome processes. J. Cell Sci. *126*, 4239–4252.

Hauf, S., Waizenegger, I.C., and Peters, J.M. (2001). Cohesin cleavage by separase required for anaphase and cytokinesis in human cells. Science *293*, 1320–1323.

Jane, F.W. (1934). Memoirs: The Structure of the Somatic Chromosomes of Alstroemeria and Bomarea. J. Cell Sci. *s2-77*, 49–75.

Keyl, H.G. (1975). Lampbrush chromosomes in spermatocytes of Chironomus. Chromosoma *51*, 75–91.

Kireeva, N., Lakonishok, M., Kireev, I., Hirano, T., and Belmont, A.S. (2004). Visualization of early chromosome condensation: a hierarchical folding, axial glue model of chromosome structure. J. Cell Biol. *166*, 775–785.

Kleckner, N. (2006). Chiasma formation: chromatin/axis interplay and the role(s) of the synaptonemal complex. Chromosoma *115*, 175–194.

Kleckner, N., Zickler, D., Jones, G.H., Dekker, J., Padmore, R., Henle, J., and Hutchinson, J. (2004). A mechanical basis for chromosome function. Proc. Natl. Acad. Sci. USA *101*, 12592–12597.

Kops, G.J., Saurin, A.T., and Meraldi, P. (2010). Finding the middle ground: how kinetochores power chromosome congression. Cell Mol. Life Sci. *67*, 2145–2161.

Kops, G.J., van der Voet, M., Manak, M.S., van Osch, M.H., Naini, S.M., Brear, A., McLeod, I.X., Hentschel, D.M., Yates, J.R., 3rd, van den Heuvel, S., and Shah, J.V. (2015). APC16 is a conserved subunit of the anaphase-promoting complex/cyclosome. J. Cell Sci. *128*, 4025.

Liang, Z., Zickler, D., Prentiss, M., Chang, F.S., Witz, G., Maeshima, K., and Kleckner, N. (2015). Chromosomes Progress to Metaphase in Multiple

Discrete Steps via Global Compaction/Expansion Cycles. Cell *161*, 1124–1137.

Llères, D., James, J., Swift, S., Norman, D.G., and Lamond, A.I. (2009). Quantitative analysis of chromatin compaction in living cells using FLIM-FRET. J. Cell Biol. *187*, 481–496.

Maeshima, K., and Laemmli, U.K. (2003). A two-step scaffolding model for mitotic chromosome assembly. Dev. Cell *4*, 467–480.

Maeshima, K., Eltsov, M., and Laemmli, U.K. (2005). Chromosome structure: improved immunolabeling for electron microscopy. Chromosoma *114*, 365–375, https://doi.org/10.1007/s00412-005-0023-7.

Maeshima, K., Imai, R., Tamura, S., and Nozaki, T. (2014). Chromatin as dynamic 10-nm fibers. Chromosoma *123*, 225–237.

Manders, E.M., Kimura, H., and Cook, P.R. (1999). Direct imaging of DNA in living cells reveals the dynamics of chromosome formation. J. Cell Biol. *144*, 813–821.

Manton, I. (1950). The spiral structure of chromosomes. Biol. Rev. Camb. Philos. Soc. *25*, 486–508.

Marko, J.F. (2011). The mitotic chromosome: structure and mechanics. In Genome Organization and Function in the Cell Nucleus, First Edition, K. Rippe, ed. (Wiley-VCH Verlag GmgH & Co. KGaA), pp. 449–485.

Marsden, M.P., and Laemmli, U.K. (1979). Metaphase chromosome structure: evidence for a radial loop model. Cell *17*, 849–858.

Mjaavatten, A., (2020). Curvature of a 2D or 3D curve (https://www.mathworks.com/matlabcentral/fileexchange/69452-curvature-of-a-2d-or-3d-curve), MATLAB Central FIle Exchange. Retrieved July 27, 2020.

Nagasaka, K., Hossain, M.J., Roberti, M.J., Ellenberg, J., and Hirota, T. (2016). Sister chromatid resolution is an intrinsic part of chromosome organization in prophase. Nat. Cell Biol. *18*, 692–699.

Nakajima, M., Kumada, K., Hatakeyama, K., Noda, T., Peters, J.M., and Hirota, T. (2007). The complete removal of cohesin from chromosome arms depends on separase. J. Cell Sci. *120*, 4188–4196.

Natsume, T., Kiyomitsu, T., Saga, Y., and Kanemaki, M.T. (2016). Rapid Protein Depletion in Human Cells by Auxin-Inducible Degron Tagging with Short Homology Donors. Cell Rep. *15*, 210–218.

Neumann, B., Walter, T., Hériché, J.K., Bulkescher, J., Erfle, H., Conrad, C., Rogers, P., Poser, I., Held, M., Liebel, U., et al. (2010). Phenotypic profiling of the human genome by time-lapse microscopy reveals cell division genes. Nature *464*, 721–727.

Ohnuki, Y. (1965). Demonstration of the spiral structure of human chromosomes. Nature *208*, 916–917.

Ohnuki, Y. (1968). Structure of chromosomes. I. Morphological studies of the spiral structure of human somatic chromosomes. Chromosoma *25*, 402–428.

Ono, T., Fang, Y., Spector, D.L., and Hirano, T. (2004). Spatial and temporal regulation of Condensins I and II in mitotic chromosome assembly in human cells. Mol. Biol. Cell *15*, 3296–3308.

Piskadlo, E., Tavares, A., and Oliveira, R.A. (2017). Metaphase chromosome structure is dynamically maintained by condensin I-directed DNA (de)catenation. eLife *6*, e26120.

Poirier, M.G., and Marko, J.F. (2002). Mitotic chromosomes are chromatin networks without a mechanically contiguous protein scaffold. Proc. Natl. Acad. Sci. USA *99*, 15393–15397.

Saitoh, Y., and Laemmli, U.K. (1994). Metaphase chromosome structure: bands arise from a differential folding path of the highly AT-rich scaffold. Cell *76*, 609–622.

Schindelin, J., Arganda-Carreras, I., Frise, E., Kaynig, V., Longair, M., Pietzsch, T., Preibisch, S., Rueden, C., Sallfeld, S., Schmid, B., et al. (2012). Fiji: an open-source platform for biological-image analysis. Nat. Methods *9*, 676–682.

Skibbens, R.V. (2019). Condensins and cohesins - one of these things is not like the other! J. Cell Sci. *132*, 132.

Strukov, Y.G., and Belmont, A.S. (2009). Mitotic chromosome structure: reproducibility of folding and symmetry between sister chromatids. Biophys. J. *96*, 1617–1628.

Strukov, Y.G., Wang, Y., and Belmont, A.S. (2003). Engineered chromosome regions with altered sequence composition demonstrate hierarchical large-scale folding within metaphase chromosomes. J. Cell Biol. *162*, 23–35.

Sumner, A.T. (1998a). The mitotic chromosome. In Advances in Genome Biology, Volume 5, R.S. Verma, ed. (Elsevier), pp. 211–262.

Sumner, A.T. (1998b). The structure of the centromeric region of CHO chromosomes. Cell Biol. Int. *22*, 127–130.

Sun, M., Biggs, R., Hornick, J., and Marko, J.F. (2018). Condensin controls mitotic chromosome stiffness and stability without forming a structurally contiguous scaffold. Chromosome Res. *26*, 277–295.

Tavormina, P.A., Côme, M.G., Hudson, J.R., Mo, Y.Y., Beck, W.T., and Gorbsky, G.J. (2002). Rapid exchange of mammalian topoisomerase II alpha at kinetochores and chromosome arms in mitosis. J. Cell Biol. *158*, 23–29.

Vassilev, L.T., Tovar, C., Chen, S., Knezevic, D., Zhao, X., Sun, H., Heimbrook, D.C., and Chen, L. (2006). Selective small-molecule inhibitor reveals critical mitotic functions of human CDK1. Proc. Natl. Acad. Sci. USA *103*, 10660–10665.

Waizenegger, I.C., Hauf, S., Meinke, A., and Peters, J.M. (2000). Two distinct pathways remove mammalian cohesin from chromosome arms in prophase and from centromeres in anaphase. Cell *103*, 399–410.

Walther, N., Hossain, M.J., Politi, A.Z., Koch, B., Kueblbeck, M., Ødegård-Fougner, Ø., Lampe, M., and Ellenberg, J. (2018). A quantitative map of human Condensins provides new insights into mitotic chromosome architecture. J. Cell Biol. *217*, 2309–2328.

Zickler, D., and Kleckner, N. (1999). Meiotic chromosomes: integrating structure and function. Annu. Rev. Genet. *33*, 603–754.

Please cite this article in press as: Chu et al., The 3D Topography of Mitotic Chromosomes, Molecular Cell (2020), https://doi.org/10.1016/j.molcel.2020.07.002



## STAR★METHODS

### KEY RESOURCES TABLE

| REAGENT or RESOURCE | SOURCE | IDENTIFIER |
|---|---|---|
| Antibodies | | |
| Mouse monoclonal anti-Topoisomerase IIα (Ki-S1) | EMD Millipore | Cat# MAB4197; RRID: AB_2205862 |
| Rabbit Polyclonal anti-NCAPH | Novus Biologicals | Cat# NBP1-88345; RRID: AB_11030410 |
| Rabbit polyclonal anti-hCapH2 | Ono et al., 2004 | N/A |
| Rabbit anti-SMC6L1 | Abcam | Cat# ab18039; RRID: AB_444204 |
| Goat polyclonal anti-HMG-I/HMG-Y(N-19) | Santa Cruz Biotechnology | Cat# sc-1564; RRID: AB_2264022 |
| Mouse monoclonal anti-BrdU (IIB5) | Santa Cruz Biotechnology | Cat# sc-32323; RRID: AB_626766 |
| Mouse monoclonal anti-c-Myc (9E10) | Santa Cruz Biotechnology | Cat# sc-40; RRID: AB_627268 |
| Alexa Fluor 488 donkey anti-rabbit IgG (H+L) | Thermo Fisher Scientific | Cat # A-21206; RRID: AB_141708 |
| Alexa Fluor 594 donkey anti-rabbit IgG (H+L) | Thermo Fisher Scientific | Cat # A-21207; RRID: AB_141637 |
| Alexa Fluor 647 donkey anti-rabbit IgG (H+L) | Thermo Fisher Scientific | Cat # A-31573; RRID: AB_2536183 |
| Alexa Fluor 488 donkey anti-mouse IgG (H+L) | Thermo Fisher Scientific | Cat # A-21202; RRID: AB_141607 |
| Alexa Fluor 555 donkey anti-mouse IgG (H+L) | Thermo Fisher Scientific | Cat# A-31570; RRID: AB_2536180 |
| Alexa Fluor 594 donkey anti-mouse IgG (H+L) | Thermo Fisher Scientific | Cat # A-21203; RRID: AB_141633 |
| Alexa Fluor 647 donkey anti-mouse IgG (H+L) | Thermo Fisher Scientific | Cat # A-31571; RRID: AB_162542 |
| Alexa Fluor 488 donkey anti-goat IgG (H+L) | Thermo Fisher Scientific | Cat # A-11055; RRID: AB_2534102 |
| Chemicals, Peptides, and Recombinant Proteins | | |
| hydroxyurea | Sigma-Aldrich | Cat#H8627; CAS: 127-07-1 |
| RO3306 | Sigma-Aldrich | Cat#SML0569; CAS: 872573-93-8 |
| Thymidine | Sigma-Aldrich | Cat#T1895; CAS: 50-89-5 |
| S-trityl-L-cysteine | Sigma-Aldrich | Cat#164739; CAS: 2799-07-7 |
| Doxycycline hyclate | Sigma-Aldrich | Cat##D9891; CAS: 24390-14-5 |
| Geneticin(G418) | Calbiochem | Cat#345810; CAS: 108321-42-2 |
| DAPI | Sigma-Aldrich | Cat#D9542; CAS: 28718-90-3 |
| Hoechst 33342 | Molecular Probes | Cat#H1399; CAS: 23491-52-3 |
| YOYO-1 Iodide (491/509) | Molecular Probes | Cat#Y3601; CAS: N/A |
| EdU | Sigma-Aldrich | Cat#900584; CAS: 61135-33-9 |
| F-ara-EdU | Sigma-Aldrich | Cat#T511293; CAS: 0000000000 |
| BrdU | TCI-EP | Cat#B1575; CAS: 59-14-3 |
| Critical Commercial Assays | | |
| Click-iT Plus EdU Cell Proliferation Kit | ThermoFisher | Cat#C10637 |
| Effectene Transfection Reagent | QIAGEN | Cat#301425 |
| TetraSpeck Fluorescent Microspheres Sampler Kit | ThermoFisher | Cat#T7284 |
| Experimental Models: Cell Lines | | |
| Human HeLa cell line | Kops et al., 2010 | N/A |
| H2B-GFP HeLa cell line | Llères et al., 2009 | N/A |

(*Continued on next page*)

Please cite this article in press as: Chu et al., The 3D Topography of Mitotic Chromosomes, Molecular Cell (2020), https://doi.org/10.1016/j.molcel.2020.07.002





*Continued*

| REAGENT or RESOURCE | SOURCE | IDENTIFIER |
|---|---|---|
| LLC-Pk EGFP–TopoIIα cell line | Tavormina et al., 2002 | N/A |
| Indian Muntjac cell line (DM87) | Manders et al., 1999 | N/A |
| Indian Muntjac mCherry-H2B cell line | this paper | N/A |
| HeLa-Scc1-9myc cell line | Hauf et al., 2001 | N/A |
| HeLa-Scc1-9myc-non cleavable cell line | Hauf et al., 2001 | N/A |
| HCT116 cell line | Natsume et al., 2016 | N/A |
| Recombinant DNA | | |
| Plasmid: pH2B-mCherry (P30632) | Neumann et al., 2010 | N/A |
| Plasmid: pEF1a-EGFP-Kleisin-β | Maeshima et al., 2014 | N/A |
| Plasmid: pEF1a-EGFP-Kleisin-γ | Maeshima et al., 2014 | N/A |
| Software and Algorithms | | |
| Fiji | Schindelin et al., 2012 | https://fiji.sc/ |
| ZEN Black software v2.6 | Zeiss | https://www.zeiss.com/corporate/int/home.html |
| ZEN Blue software v2.6 | Zeiss | https://www.zeiss.com/corporate/int/home.html |
| Volocity | PerkinElmer | https://www.perkinelmer.com/ |
| Imaris | Bitplane | https://imaris.oxinst.com/ |
| PyMOL | Schrödinger | https://pymol.org/2/ |
| MATLAB 2018 | MathWorks | https://uk.mathworks.com/ |
| Excel | Microsoft | https://www.microsoft.com/microsoft-365 |
| GraphPad Prism 8 | GraphPad Software | https://www.graphpad.com/scientific-software/prism/ |
| AutoQuant X | Media Cybernetics | https://projects.iq.harvard.edu/kleckner_lab/lab-software |
| Centroid Path Determination and Analysis | Kleckner laboratory | |

## RESOURCE AVAILABILITY

### Lead Contact

Further information and requests for resources and reagents should be directed to Nancy Kleckner at kleckner@fas.harvard.edu.

### Materials Availability

This study did not generate new unique reagents. Cell lines transiently containing plasmids were not stored and can be reconstructed from previously existing reagents.

### Data and Code Availability

#### *Software Availability*

The program for centroid path determination and analysis, written in MATLAB, is available at https://projects.iq.harvard.edu/kleckner_lab/lab-software.

## EXPERIMENTAL MODEL AND SUBJECT DETAILS

### Cell Lines

Human HeLa histone H2B-GFP cell line and pig LLC-Pk EGFP-TopIIα cell line were gifts from D. Llères (Llères et al., 2009) and G. Gorbsky (Tavormina et al., 2002), respectively. HeLa-Scc1-9myc cell line and HeLa-Scc1-9myc-non cleavable cell lines were gifts from J.M. Peters (Hauf et al., 2001). The native DM87, HeLa, and HCT116 cell lines were gifts from P. Cook (Manders et al., 1999), J. Shah (Kops et al., 2015) and M. Kanemaki (Natsume et al., 2016), respectively. The Indian Muntjac mCherry-H2B cell line was constructed by transfecting DM87 cells with a pH2B-mCherry plasmid (a gift from Jan Ellenberg) (Neumann et al., 2010) and selecting with 1 μg/μl Geneticin (Calbiochem, 345810). In some experiments, DM87 cells and HeLa cells transient co-express H2B-mCherry and EGFP-Kleisin-β or EGFP-Kleisin-γ after co-transfection with pH2B-mCherry and pEF1a-EGFP-Kleisin-β or

Please cite this article in press as: Chu et al., The 3D Topography of Mitotic Chromosomes, Molecular Cell (2020), https://doi.org/10.1016/j.molcel.2020.07.002



pEF1a-EGFP-Kleisin-γ plasmids (the latter were gifts from Kazuhiro Maeshima) (Maeshima et al., 2014). The transient transfection protocol was executed using Effectene Transfection Reagent (QIAGEN, 301425) according to manufacturer's manual.

### Standard Growth Conditions

Cells were grown in Dulbecco's modified Eagle's medium (DMEM; Life Technologies) with 10% fetal bovine serum (FBS, VWR), 2 mM L-glutamine and 100 units/ml penicillin plus 100 μg/ml streptomycin (Life Technologies), at 37°C with 5% CO2 in a humidified incubator.

## METHOD DETAILS

### Synchronization and Inhibitor Treatments

For live cell imaging of LLC-Pk (pig) cells, cells were synchronized at G2/prophase boundary by incubating cells with 9 μM CDK1 inhibitor RO3306 (Sigma-Aldrich, SML0569) for 20 hours (Vassilev et al., 2006) and released by washing out the inhibitor with DMEM. Cells enter prophase within 1 hr after release. For all DM87 cell studies, cells were synchronized with 2 mM hydroxyurea (Sigma-Aldrich, H8627) at the G1/S boundary for 20 hr. Cells reach mitosis ~7 hr after release. For all HeLa cell experiments, cells were synchronized at the G1/S boundary by treatment with 2 mM thymidine (Sigma-Aldrich, T1895) for 24 hr and released by washing out the inhibitor with DMEM. Cells enter mitosis at ~7 hr after release.

For analysis of Scc1-9myc expression (Figures 2G and 2H), cells were induced with 1 μg/ml of Doxycycline (Sigma-Aldrich, D9891) for 48 hr before fixation (Hauf et al., 2001).

For imaging of Scc1-9myc-non-cleavable cells (Figures 2I and S2A), cells were transfected with pH2B-mCherry, further incubated for 8 hr, and then treated with 2 mM Thymidine for 20 hr to give synchronization at the G1/S boundary. At the time of release from arrest, Doxycycline was added to a final concentration of 1 μg/mL and cells further incubated and then imaged after an additional 12 hr.

For EdU labeling (Figures 2L, top, and S2E), DM87 cells were synchronized with 2mM hydroxyurea for 20 hr, followed by release and treatment with 5 μM EdU (Sigma-Aldrich, 900584) for 7 hours and then fixed.

To obtain F-ara-EdU/BrdU labeled chromosomes (Figure 2M), low toxicity F-ara-EdU was used (Vassilev et al., 2006). DM87 cells were cultured in the presence of 8 μM F-ara-EdU (Sigma-Aldrich, T511293) for 4 days and then synchronized at G1/S boundary with 2 mM hydroxyurea for another 24 hr. After release from hydroxyurea, cells were treated with 30 μM BrdU (TCI-EP, B1575) for 10 hr. Then these cells were subsequently released into F-ara-EdU/BrdU- free medium and cultured for 20 hr before fixation. To enrich more mitotic chromosomes for spread, cells were treated with 20 μM S-trityl-L-cysteine (STLC, Sigma-Aldrich, 164739) for 12 hr.

### Sample Preparation

#### *Fixed Whole Cells*

Whole cells were fixed by one of two methods: (1) Methanol fixation (Figures 1J, 2E, 2F, 2L, top, 3P, 4A, 4B, 5B, 5D, 5E, 5G, S1D, S1J, S1K, S2E, S3C, right, S4 (line 9-10,19-21), S5E, bottom, and S5F, left). Cells were rinsed in 1xPBS (Phosphate Buffered Saline) (137 mM NaCl, 2.7 mM KCl, 10 mM Na2HPO4, 1.8 mM KH2PO4, pH 7.4) and then fixed in pre-chilled 100% methanol for 20 min at −20°C. (2) "Pre-extraction" fixation as in (Hauf et al., 2001; Liang et al., 2015). Cells were rinsed with 0.1% Triton X-100 in HMK buffer (20 mM HEPES, pH 7.5, 1 mM MgCl2, 100 mM KCl) and, after 1-2min, fixed by treatment either with pre-chilled 100% methanol for 20 min at −20°C (Figures 1A right and 1B right) or with 3.7% paraformaldehyde for 10 min (Figures 1K, 2B, 2D, 2G, S1B, S1H, S1I, S1M, and S4 (line 8)). Following fixation, cells were rinsed with PBS, permeabilized with 0.01% (v/v) Triton X-100 in PBS (PBST) for 5 min and incubated in 5% BSA in PBST for 2 hr.

### Spread Chromosome Preparations

Cells were collected after trypsinization, suspended in in hypotonic buffer of 50% culture medium in water for 5.5 min, and then fixed in freshly made pre-cold 3:1 methanol-acetic acid (Figures 2L, bottom, 2M, 3K, S1C, S2G, and S4 (line 4-7,11-18)) (Giménez-Abián et al., 1995). Aliquots of the fixed sample were then dropped on slides and air-dried.

### Immuno- and/or DNA staining

For immunostaining, whole or spread cell preparations were incubated with the primary antibodies overnight at 4°C, or 1 hr at room temperature. After washing in PBST three times, cells were incubated for 1 hr at room temperature with secondary antibodies. As desired, cells were then stained with 1 μg/ml 4',6-diamidino-2-phenylindole (DAPI, Sigma-Aldrich, D9542) in PBS for 10 min, or 0.1 μM YOYO1 (Molecular Probes, Y3601) in PBS for 10 min before mounting with ProLong Gold anti-fade reagent (Life Technologies).

Primary antibodies: monoclonal mouse anti-TopIIα (Millipore, MAB4197) at 1:100; polyclonal rabbit anti-hCapH at 1:50 (Novus, NBP1-88345); polyclonal rabbit anti-hCAPH2 at 1:500 (a gift from Tatsuya Hirano, Japan); rabbit anti-SMC6L1 at 1:50 (Abcam, ab18039); polyclonal anti-HMG-I/HMG-Y(N-19) at 1:50 (Santa Cruz, sc-1564); monoclonal mouse anti-BrdU Antibody (IIB5) at 1:400 (Santa Cruz, sc-32323); and monoclonal mouse anti-c-Myc Antibody (9E10) at 1:400 (Santa Cruz, sc-40).

Please cite this article in press as: Chu et al., The 3D Topography of Mitotic Chromosomes, Molecular Cell (2020), https://doi.org/10.1016/j.molcel.2020.07.002



The following secondary antibodies were used in this study (all at 1:400 dilution): Alexa Fluor 488 donkey anti-mouse IgG (H+L) antibody (Thermo Fisher Scientific, A-21202), Alexa Fluor 555 donkey anti-mouse IgG (H+L) antibody (Thermo Fisher Scientific, A-31570), Alexa Fluor 594 donkey anti-mouse IgG (H+L) antibody (Thermo Fisher Scientific, A-21203), Alexa Fluor 647 donkey anti-mouse IgG (H+L) antibody (Thermo Fisher Scientific, A-31571), Alexa Fluor 488 donkey anti-rabbit IgG (H+L) antibody (Thermo Fisher Scientific, A-21206), Alexa Fluor 594 donkey anti-rabbit IgG (H+L) antibody (Thermo Fisher Scientific, A-21207), Alexa Fluor 647 donkey anti-rabbit IgG (H+L) antibody (Thermo Fisher Scientific, A-31573). Alexa Fluor 488 donkey anti-goat IgG (H+L) antibody (Thermo Fisher Scientific, A-11055).

For EdU-BrdU labeled chromosomes, spread chromosome samples were incubated with 1 M HCl for 10 min on ice and with 2 M HCl for 10 min at room temperature, and then neutralized with phosphate/citric acid buffer (0.2 M Na2HPO4, 0.1 M citric acid, pH 7.4) for 10 min at room temperature. After washing and blocking, cells were incubated with BrdU antibodies diluted in 5% BSA in PBST for 1 hr. Incorporated F-ara-EdU was detected with Alexa Fluor 488 Azide by Click-iT EdU imaging kits (ThermoFisher, C10637).

## Imaging and Data Collection

### *Fixed samples imaging*

Fixed samples were imaged in one of three different ways:

- Samples in Figures 1J, 2B, 2G, 2L, bottom, 3K, S1D, S1H, S1M, S2G, and S4 (lines 8-14) were imaged with Structured Illumination Microscopy (SIM) using a 100x/1.4 NA Plan-Apochromat objective on an Elyra PS.1 microscope (Carl Zeiss). Fluorescence excitation was provided by 405, 488 and 561 nm diode lasers and an Andor EMCCD 1024 × 1024-pixel camera was used for detection. Stripe-based SIM illumination was utilized. Stripes were moved laterally five times at five different angles (rotations). Stage movement in Z was performed using a Z-Piezo system. Three-dimensional images were acquired with a raw voxel size of 0.05 × 0.05 × 0.08 μm and an updated voxel size of 0.03 × 0.03 × 0.08 μm after processing. Raw data was processed using Zeiss' ZEN Black software version 2.6.
- Samples in Figures 1K, 2D, 2E, 2M, 3P, S1B, S1C, S1I, S1J, S3C, right, S4 (lines 1-8,15-21), S5A, S5B, S5D–S5F, and S6A–S6D were imaged with a LSM880 confocal microscope equipped with an Airyscan detector (Carl Zeiss) A 63x/1.4 NA Plan-Apochromat objective was used. Excitation light was from a 405 nm diode laser, 488 nm Argon laser or a 561 nm DPSS laser. Fluorescence was detected via the Zeiss Airyscan 32-channel GaAsP PMT array detector in super-resolution (SR) mode. Three-dimensional images were acquired in LineSequential Scan mode for single channel imaging, in Frame Scan model for two channels imaging, with 16 Bit depth and a raw voxel size 0.04 × 0.04 × 0.19 μm. The picture voxel sizes were the same after processing. Raw data was processed using Zeiss' ZEN Black software version 2.6.
- Images in Figures 1A, right, 1B, right, 2F, 2L, top, 4A, 4B, 5D, 5E, S1K, and S2E were taken with an inverted Nikon Ti wide field epi-fluorescence microscope. Images were collected using MetaMorph (Molecular Devices). Images were subjected to 1x deconvolution except Figures 4A, 4B, 5D, 5E (10x), S2L, top, and S4D (20x)

## Live-cell Imaging

Cells were cultured on poly-lysine coated glass-bottom dishes (MatTek), FluoroBrite DMEM without phenol red (Life Technologies) with 10% FBS, 2 mM L-glutamine and 100 units/ml penicillin plus 100 mg/ml streptomycin. In some cases, cells were incubated with 0.1 μg/ml Hoechest 33342 (Molecular Probes, H1399) for 5 min and washed with 1x PBS for three times, prior to the observation.

Snapshots (Figures 1I, 2A, 2C, 2K, 3A, 3C, 3Q, 5C, 5H, 5I, 6K, S1A, S1E–S1G, S1L, S2C, S2D, S2F, second row, S3C, left, S4 (line 1-3), S5A, S5B, S5D, S5E, top, and S5F, right) and real-time imaging (Figures 2I, 6E, 6I, 6M–6O, S6A, S6C, and S6D) of living cells were performed with the LSM880+Airyscan confocal microscope described above. Samples were placed in a heated stage-top incubator (37°C) that was continually flooded with humidified air that was pre-warmed (37°C) and mixed with 5% CO2. Further, the upper portion of the microscope stand was enclosed in a heated plexiglass chamber (37°C). Images were acquired at 30 s, 5 min or other intervals or snapshots.

All raw data for the above experiments was processed using Zeiss' ZEN Black software version 2.6. For analysis of individual chromosomes, the relevant region from the z stack extracted by cropping using Fiji and rotated as appropriate to produce a single chromosome stack. In general, chromosome examples selected for analysis were co-planar with the XY imaging plane.

DM87 DNA live cell snapshot pictures (Figures 1A, left, 1B, left, 2J, and S2B) were taken on a Nikon-Ti inverted microscope equipped with a 100x/1.4NA oil emersion objective, Prior Lumen 200 excitation source, Nikon PerfectFocus system to eliminate Z drift, and an Andor Cascade II EMCCD camera. Z stacks were collected using a Prior NanoScanZ Nanopositioning Piezo Z Stage System. Slice separation ranged from 200 nm with 100–300 ms exposure time per slice, and typically covered a range of 20 μm. Samples were placed in a heated stage-top incubator (37°C) that was continually flooded with humidified air that was pre-warmed (37°C) and mixed with 5% CO2. Slice separation ranged from 200 nm with 100–300 ms exposure time per slice, and typically covered a range of 20 μm for mammalian cells. Cells were incubated in DMEM with 0.1 μg/ml Hoechst 33342 for 5 min, washed three times with medium prior to imaging as (2). The pictures are deconvolved 1x iteration using AutoQuant (Media Cybernetics, Inc.) with appropriate point spread functions. Images were subjected to 1x deconvolution except Figure 2J (10x).

Please cite this article in press as: Chu et al., The 3D Topography of Mitotic Chromosomes, Molecular Cell (2020), https://doi.org/10.1016/j.molcel.2020.07.002



### Measurement of Distances

Measurement of inter-bridge distances, inter-bubble distances and bubble sizes (Figures 3F, 4E, 6B, and S4).

*Inter-bridge distances:* distances between Top IIα bridges were determined in fixed, spread preparations, in fixed whole cells and in living whole cells (Figure S4). See Methods S1, Protocol 1 for examples about measuring the inter-bridge distances.

*Distances between bubbles and bubble lengths* were determined from the same types of preparations as for bridges. See Methods S1, Protocol 2 for examples about measuring distances between bubbles and bubble lengths.

***Chromosome length measurements*** (Figures 6A, S6A, and S6B). Cells plated on poly-lysine coated glass-bottom dishes (MatTek) were treated with RO3306 for 20 hours, and after release for 1h, pictures were taken at 1 min interval from late prophase to anaphase, from the cell top to cell bottom, using Zeiss880+Airyscan. Chromosome length were analyzed using IMARIS. It is not possible to measure all the chromosomes, so by choosing three clearly distinguishable chromosomes, we could trace their lengths as the cell progresses with the IMARIS Filament function.

Analysis of unsplit axis deformation (Figures 4C and 4D)

Visual inspection of images of mid- and late prophase nuclei (e.g., Figures 4A and 4B) allows categorization of 1.2-1.5 μm unsplit axis segments into smoother and more deformed shapes according to whether the maximum deviation of the center line of the shape from a linear baseline is less or more than ± 3 pixels (Figure 4C left and right, respectively). Figure 4D: the frequency of more deformed segments is higher in late prophase nuclei than in mid-prophase nuclei (defined by presence and absence of split axes, N = 7 and 9 nuclei, respectively). Note: progression to more deformed shapes are likely greater than it appears because axes with increased deformation are constantly being converted to split axis forms.

### Image Analysis and Presentation

#### *Channel alignment*

Channel alignment in three fluorescence channels was implemented using 0.5 μm diameter multi-color beads (TetraSpeck Fluorescent Microspheres Sampler Kit, ThermoFisher, T7284). Beads were sonicated and dried onto a slide. Images taken in DAPI, FITC, and Cy3 channels were co-aligned using ZEN channel alignment software (Carl Zeiss).

### Z direction correction

Z direction correction was performed using 0.5 μm diameter multi-color beads. In one approach, inter-plane distance was adjusted using the appropriate PSF. In a second approach, the 3D bead image was created using ImageJ and the inter-plane distance was adjusted manually until the diameter of the bead was the same in the Z dimension as in the X and Y dimensions. The same correction factor emerged by both methods. All 3D analyses were based on appropriately corrected Z stack images.

### Determination of centroid paths

The centroid paths of chromosome axis shapes and chromatin shapes (Figures 3C, 3E, 3G, 3I, 3N–3Q, 5B–5E, 5G–5I, 6F, bottom, 6I, second row, 6L, middle row, S2F, top, S3C, S5A, S5B, S5D, and S5F) were defined with a home-made algorithm that uses an intensity-weighted centroid computation. See Methods S1, Protocol 3 for the method to determine centroid paths.

### Centroid analysis for different sub-stages

Centroid analysis was subjected to sample pre-preparation. See Methods S1, Protocol 4 for the example about pre-preparing the samples.

***Unsplit prophase shapes*** (Figures 5B–5E, S5D, and S5F). The centroid paths for unsplit prophase axis shapes were analyzed with the centroid analysis MATLAB code. Four factors were set. (1) The xyz scales are described by a 3-element vector containing the scale conversions for X, Y, and Z coordinates in pixels/micron. This was set at the default: [1 1 1]. (2) The sfactor, the smoothing factor when computing pitch. This is roughly what a simple/naive forward-difference derivative would return, and we set it at the default value of 1. (3) The normvolreject is the rejection volume fraction. The analysis will reject any 3D objects it finds to have less than normvolreject of the total volume. We use the default value of 0.07. (4) The watershed_threshold is a manually defines a threshold for the watershed rejection minimum, we use the default value of 10. The new centroid information data was produced and saved with "save_for_pymol" function (see "README" detailly in the attached centroid code), the produced sphere position data were used for further analysis, including transfer to PyMOL for 3D centroids rendering. The DNA-axis superimposed centroids pictures were determined separately and then reunited.

### Centroid analyses of split shapes

For shapes that are split along their entire lengths (Figures 3C, 3E–3G, 3I, 3N–3Q, 5I, 6F, bottom, 6I, second row, 6L, middle row, S5A, and S5B), the regions corresponding to each of the two sisters were defined by appropriate cropping along the "midline" of the axis shape. These cropped single-sister regions were then used for analysis of both axis and chromatin shapes. Centroid analysis was carried out using the same default parameters as for unsplit shapes (above). For late prophase shapes with partial splitting, i.e., bubbles or splitting forks (Figures 5G and 5H), the centroid path of the unsplit region and the centroid paths of the bubble/branch regions (divided into two parts corresponding to the two sisters as above) were determined separately and then reunited. 3D PyMOL centroids rendering was performed by inputting the centroid information data (one/two axes) produced by centroids algorithm. The DNA-axis superimposed centroids pictures were determined separately and then reunited.

Please cite this article in press as: Chu et al., The 3D Topography of Mitotic Chromosomes, Molecular Cell (2020), https://doi.org/10.1016/j.molcel.2020.07.002





### Analysis of axis centroid paths

#### *Contour lengths of handedness segments (Figures 3D, 5F, S3A, S3B, S3E, and S3F)*

The contour length of a segment of given handedness is given by the corresponding the number of slices as defined by the centroid path algorithm (above), multiplied by the depth of the slice (i.e., one pixel).

***Comparison of left- and right-handedness lengths*** (Figure S3G) was made by summing the total number of slices (pixels) of each handedness for the centroid paths of the desired group of axis images.

### Comparison of handednesses between split sister axes (Figures 6H and S3H)

For each late prophase chromosome, the centroid paths of sister axes were phased by eye. Then, for each corresponding slice (pixel) position, handedness comparisons were defined as both R, both L, or different (RL or LR) and the totals for each category presented.

### Curvature magnitudes of centroid paths (Figures 5K and 5L)

Centroid paths are given as list of $x$, $y$ and $z$ coordinates with every point of the path defined as $\mathbf{P}_i = [x_i, y_i, ]$. The circle passing through all three corners of the triangle formed by the neighboring points $\mathbf{P}_{i-n}$, $\mathbf{P}_i$ and $\mathbf{P}_{i+n}$ is used to calculate the curvature at $\mathbf{P}_i$, n being a distance from $\mathbf{P}_i$ in pixels. $\boldsymbol{M}_i$ is the center and $R_i$ is the radius of this circle. The curvature of the path at $\mathbf{P}_i$ is defined as $\kappa_i = 1/R_i$. The curvature vector $\mathbf{k_i}$ is defined as the vector of length $\kappa_i$ in the direction from $\mathbf{P}_i$ to $\boldsymbol{M}_i$. $\kappa_i$ were calculated at every point of centroid paths using MATLAB script (Mjaavatten, 2020) and plotted as histograms normalized with probability function.

### PyMOL renderings and PyMOL-centroids superimposition

All 3D renderings of whole axis and/or chromatin shapes and/or their centroids in Figures 3C, 3E, 3G, 3I, 3J, 3N–3Q, 5B–5E, 5G–5I, 6F, bottom, 6I, second row, 6L, middle row, S2F, top row, S3C, S5A, S5B, S5D, and S5F were accomplished in PyMOL (https://www.pymolwiki.org/index.php/Tiff2ccp4; D. Jeruzalmi and J. Vertrees). For whole shapes, the visualized object is an iso-intensity surface contour that defines the volume encompassing signals whose signals are at or above a defined threshold. The surface-centroids superimposition was performed by inputting the centroids information data produced by centroids algorithm into the surface rendered PyMOL pictures.

### Intensity contour analysis and contour-centroid superimposition

For a chromosome of interest (Figure 3A), longitudinal slices along appropriately oriented chromosomes were obtained using the Fiji Reslice function. Individual cross-section planes were extracted, and contour analysis was performed using the contour analysis function from MATLAB: https://www.mathworks.com/help/matlab/ref/contour.html. 4 contour levels were used: 0.6*dmax, 0.7*dmax, 0.8*dmax and 0.9*dmax.

### Axis, shape and bridge dynamics analysis (Figures 6D–6F and 6I–6K)

3D single chromosome images were taken at 15 s intervals at 37°C (Figures 6D-6F) or 20°C (Figures 6I–6K). For bridges dynamics analysis (Figures 6D–6F), bridges were viewed in the single middle plane of the Z stack and positions of bridges defined by intensity profiles along the midline of the shape (Figure 6D), which correspond directly to bridge positions as defined by eye. Chromosome lengths in Figure 6F were defined as the contour lengths of the corresponding centroids. For axis dynamics (Figures 6I–6K), axis centroids were defined and superimposed on Pymol renderings (Figure 6I). Handedness patterns were represented in linear form by red/blue bars (Figures 6G and 6I).

### Volocity and Imaris 3D renderings

Certain 3D renderings of whole axis or chromatin shapes, i.e., in Figures 6I, top rows, 6M–6O, S6C, and S6D, were performed with Volocity (PerkinElmer). The visualized object is an iso-intensity surface contour that defines the volume encompassing signals whose signals are at or above a defined threshold. The chromosome axis 3D rendering in Figures S6A and S6B were performed with Imaris (Bitplane).

### Statistical Analysis

#### *Gamma fitting analysis*

Distributions of inter-bridge and inter-bubble distances (Figures 3F, 4E, 6B, and S4) were plotted with MATLAB 2018a (The MathWorks, Inc). Distributions were fitted with a gamma function from the 99% confidence interval. The data means and their standard deviations were calculated with MATLAB.

### Two-Gaussian analysis of left and right handedness segments (Figures 3D, 5F, S3A, S3B, S3E, and S3F)

Distributions of lengths of segments of left- and right-handedness from axis centroids were plotted with MATLAB 2018a (The MathWorks, Inc). Distributions were reasonably well fit with a bimodal Gaussian distribution but not unimodal Gaussian distribution (not shown). The probability, data means, and their standard deviations were calculated with MATLAB.